

## A MAGELLAN IMACS SPECTROSCOPIC SEARCH FOR Ly $\alpha$ EMITTING GALAXIES AT REDSHIFT 5.7

CRYSTAL L. MARTIN<sup>1</sup>

University of California, Santa Barbara

Department of Physics

Santa Barbara, CA, 93106

cmartin@physics.ucsb.edu

AND

MARCIN SAWICKI

St. Marys University

Department of Astronomy and Physics

923 Robie Street

Halifax, N.S., B3H 3C3, Canada

AND

ALAN DRESSLER AND PAT MCCARTHY

OCIW, Santa Barbara Street, Pasadena, CA

*To appear in ApJ.*

### ABSTRACT

We present results from a blind, spectroscopic survey for  $z \sim 5.7$  Ly $\alpha$ -emitting galaxies using the Inamori Magellan Areal Camera and Spectrograph. A total of  $\sim 200$  square arcminutes were observed in the COSMOS and LCIRS fields using a narrowband filter, which transmits between atmospheric emission lines at 8190Å, and a mask with 100 longslits. This observing technique provides higher emission-line sensitivity than narrowband imaging and probes larger volumes than strong lensing. We find 170 emission-line galaxies and identify their redshifts spectroscopically. We confirm three Ly $\alpha$  emitting galaxies (LAEs), the first discovered using multislit-narrowband spectroscopy. Their line profiles are narrow, but fitted models suggest intrinsic, unattenuated widths  $\sim 400$  km s<sup>-1</sup> FWHM. The red wing of the line profiles present features consistent with galactic winds. The star formation rates of these galaxies are at least 5-7 M<sub>⊙</sub> yr<sup>-1</sup> and likely a factor of two higher. We estimate the number density of  $L \geq 5 \times 10^{42}$  ergs s<sup>-1</sup> LAEs is  $9.0_{-4}^{+12} \times 10^{-5} h_{70}^3$  Mpc<sup>-3</sup> at redshift 5.7 and constrain the Schechter function parameters describing this population. Galaxies fainter than our detection limit may well be the primary source of ionizing photons at  $z \sim 6$ . We argue, however, that the break luminosity  $L_{*,Ly\alpha}$  is not yet well constrained. If this break luminosity is near our detection limit, and somewhat lower than previous estimates, then the detected LAE population could be responsible for ionizing the intergalactic gas at redshift  $z \sim 6$ . We discuss the potential of multislit-narrowband spectroscopy for deeper emission-line surveys.

*Subject headings:* galaxies: high-redshift – galaxies: luminosity function – techniques: spectroscopic – line: identification – line: profile

### 1. INTRODUCTION

Reionization of the intergalactic medium (IGM) marks a phase transition in the baryonic component of the universe and quite likely heralds the emergence of the first galaxies that sustain star formation beyond a single burst (Oh & Haiman 2001). The appearance of complete Ly $\alpha$  absorption troughs in quasar spectra at  $z \gtrsim 6$  shows that at least 1 in  $10^4$  hydrogen atoms was still neutral then (Becker et al. 2001; Djorgovski et al. 2001; Fan et al. 2002; Songaila 2004; Fan et al. 2006), although much of the IGM appears to have been ionized by  $z \sim 6.5$  (Becker et al. 2006, 2007). The Thomson optical depth measured from the microwave background polarization suggests an earlier start to reionization at  $z_r = 11_{-3}^{+3}$  (Page et al. 2006; Spergel et al. 2007). The Ly $\alpha$  emission line, surprisingly, is proving very useful for identifying galaxies over this protracted period

of Reionization (Iye et al. 2006; Stark et al. 2007b). Frequency shifting across the Stromgren spheres of the sources allows a fraction of the emission line photons to propagate through an IGM with a considerable neutral fraction. Understanding the intrinsic evolution of Ly $\alpha$  emitters (LAEs) builds a foundation for using the apparent evolution of the LAE luminosity function during reionization to measure the changing neutral fraction (Malhotra & Rhoads 2004; Kashikawa et al. 2006).

High-redshift LAEs may provide the first glimpse of primeval galaxies, owing to the high Ly $\alpha$  equivalent-width of young, metal-poor galaxies (Malhotra & Rhoads 2002; Dawson et al. 2004; Schaerer 2007). The stellar mass density at  $z \sim 5$  (Stark et al. 2007a), the presence of carbon in the IGM at  $z = 5.7$  (Simcoe 2006; Ryan-Weber, Pettini, & Madau 2006), and the steep faint-end slope of the

<sup>1</sup> Packard Fellow

i-dropouts (Bouwens et al. 2007) can all be interpreted as evidence for a significant population of as yet undetected dwarf galaxies at high redshift. The properties of these low-mass galaxies during and just after reionization are cosmologically important. Finding them and measuring their properties will continue to be of interest well into the next decade.

Finding high-redshift galaxies remains largely a contrast problem with the sky. Selection by Ly $\alpha$  emission provides higher sensitivity than continuum break identification for populations with large line equivalent widths, like young, metal-poor galaxies. Over the past decade, several tens of LAEs have been confirmed near redshift 6 among objects found via narrowband imaging (Hu et al. 2002; Cuby et al. 2003; Ajiki et al. 2003; Kodaira et al. 2003; Hu et al. 2004; Rhoads et al. 2004; Ajiki et al. 2004; Taniguchi et al. 2005; Shimasaku et al. 2006; Kashikawa et al. 2006; Murayama et al. 2007; Westra et al. 2005, 2006; Ouchi et al. 2007). The redshifts of nearly all of these galaxies shift the Ly $\alpha$  line into one of the bandgaps in the OH (hydroxyl) spectrum of the terrestrial sky. The dark regions at 8200Å and 9200Å are the widest ( $\sim 150\text{\AA}$ ) and are useful for studying the end of reionization. Lyman-alpha emission at  $z = 5.7$  and  $6.5$  redshifts into these bands.

Spectroscopic surveys also benefit from these low background regions and offer higher sensitivity than narrowband imaging. Dispersion of the background improves line-to-sky contrast, although a smaller solid angle of sky is covered. One prolific spectroscopic approach has been targeting strongly lensed LAEs. Probing comparatively tiny volumes, three very faint LAEs have been confirmed with this technique at  $z \sim 5 - 6$  (Ellis et al. 2001; Santos et al. 2004). Using the Hubble Space Telescope to get above the atmospheric OH emission has also produced 3 LAEs at  $z > 5$  (Pirzkal et al. 2007). Serendipitous discoveries have also been made in the “sky region” of longslit spectra (Sawicki et al. 2007; Stern et al. 2007). In this paper, we present the first detections of LAEs with a technique – multislit-narrowband spectroscopy (MNS) – designed to optimize the sensitivity of ground-based telescopes to high-redshift LAEs. Previous surveys with MNS failed to find any LAEs (e.g. Crampton & Lilly 1999; Martin & Sawicki 2004; Tran et al. 2004).

Observations were made with the Inamori Magellan Areal Camera and Spectrograph (IMACS, Dressler et al. 2006) on the Baade Telescope, which offered a wide field of view. Longslit spectra were obtained in the dark region at 8200Å. A custom blocking filter and “Venetian blinds” mask multiplexed the effective area one-hundred fold. We carried out four blind searches: two in the COSMOS (Cosmic Evolution Survey) field and two in the LCIRS (Las Campanas Infrared Survey) field. The total survey area of 200 square arcminutes is significantly larger than that attempted previously with similar techniques.

We describe the survey in §2 and explain how we found emission-line objects and identified their redshifts in §3. Some readers may wish to skip directly to §4, where we discuss the star formation and feedback properties of the LAEs, estimate their space density, and explore the contribution of the LAE population to the ionization of the IGM at  $z = 5.7$ . We summarize the advantages and disadvantages of MNS in §5, including a direct comparison to

planned instrumentation for the next generation of telescopes. Section 6 summarizes our conclusions. Properties of the foreground line-emitters will be discussed in a separate paper. We adopt a cosmology with  $\Omega_m = 0.3$ ,  $\Omega_\Lambda = 0.7$ ,  $H_0 = 70 \text{ km s}^{-1} \text{ Mpc}^{-1}$ , and  $\Omega_b h^2 = 0.02$  throughout this paper. The angular scale at redshift 5.7 is then  $5.87 \text{ kpc}''$ ; the universe is 0.98 Gyr old; and the time between redshift 6.5 and 5.7 is 151 Myr.

## 2. OBSERVATIONS AND DATA ANALYSIS

Four types of data were used in our emission-line survey. We began with the blind, emission-line survey with the IMACS instrument on the Baade telescope. Broad bandpass spectroscopy of emission-line objects was then obtained to identify the redshift of the line via the presence (or absence) of other lines. A subsample of LAE candidates was then followed up with higher-resolution spectroscopy to determine the shape of the line profile. Broadband imaging of our two fields by the COSMOS (Scoville et al. 2007; Taniguchi et al. 2007) and the LCIRS (Marzke et al. 1999; Chen et al. 2002) supplement our new spectroscopic observations. The photometric redshifts from COSMOS (Mobasher et al. 2007) were particularly useful because the association of a line-selected object with a continuum source is often ambiguous.

### 2.1. Multislit, Narrowband Spectroscopic Search

Multislit narrowband spectroscopy remains a relatively new technique, and we illustrate the filter transmission in Figures 1 and the mask design in Figure 2. Our custom blocking filter fabricated by Barr Associates passes a  $121 \text{ \AA}$  FWHM bandpass at  $8188 \text{ \AA}$ . The transmission is over 90% across this band and drops sharply to less than 5% transmission outside the  $\lambda 8104 - \lambda 8273$  bandpass. We placed this filter in the parallel beam directly in front of the  $200 \text{ lines mm}^{-1}$  grism and recorded data with the short,  $f/2$ , camera. With a dispersion of  $2.0 \text{ \AA pix}^{-1}$ , we fit spectra from 100 longslits (numbered 9 to 108) on the eight  $2\text{k}$  by  $4\text{k}$  thinned, SITe detectors. At low dispersion, the angle between the first-order spectrum and the zero-order image of the mask is smaller than the detector, so a zero-order image of the mask also falls on the detector. This zero-order image is easily recognized via the pattern of the multislit mask, and this region is masked and ignored in the analysis. The  $1''.5$  wide slits subtend a geometric area of  $55.3 \text{ \AA}^2$  per pointing within the  $27''.50$  diameter field of the camera. With this setup, emission lines from diffuse sources have a width of  $12.8 \pm 0.3 \text{ \AA}$  FWHM. The spectral resolution is typically a factor of two better for spatially-unresolved objects, as determined by the atmospheric seeing.

Table 1 summarizes the search observations. Two masks were exposed in each of two fields. The masks were offset by half the slit separation. Exposure times ranged from 6 to 11 hours, and the image quality was generally  $0''.8$  FWHM or better. Image quality was good across the detector during the 2005 March and May runs, which used the field corrector and atmospheric dispersion compensator. The 2004 April run took place prior to installation of the ADC/corrector, and the image quality was further compromised by an un-even focus across the detector caused by a misaligned tertiary mirror.

We used techniques standard to optical *imaging* to remove the instrumental signature from the data. The bandpass is narrow enough to ignore the wavelength dependence of the detector response; and we corrected for pixel-to-pixel response variations with direct images of the flat-field screen taken through the NB8190 filter (in the filter wheel). Stacked images were constructed using cosmic ray masks. Faint, sky lines are present even in the relatively clean, dark bandpass at 8200Å. We subtracted this sky background after computing it in a local aperture along the slit direction. Subtraction of this sky model revealed the objects. These procedures were implemented with a set of custom scripts, implemented with PerlDL<sup>2</sup> and IRAF routines.<sup>3</sup>

We used the location of each object along the slit and the transformation from mask to sky coordinates, kindly provided by K. Clardy, to determine object positions in the spatial direction. We tested the accuracy of the *relative astrometry* using bright, foreground objects that fell on slits and the broadband images described below. The position errors along the slit were normally distributed with standard deviation of 0''24 for the 2004 data, slightly less for the 2005 observations. The same bright objects present offsets perpendicular to the slit of  $\pm 0''36$  ( $1\sigma$  result). We emphasize, however, the degeneracy between the position of an object in the slit and the wavelength of the emission line that we measure. Half a slit width is  $\pm 0''75$ , and offsets approaching this limit lead to wavelength errors  $\leq 7.5\text{\AA}$ . The *accuracy of the zero-point* of the astrometric transformation was estimated by comparing the coordinates of the mask alignment stars, taken from the USNO catalog, to their coordinates in the Subaru images of the COSMOS field. After rejection of two stars, we find a systematic offset of 0''40 W and 0''29 S of the Subaru positions using four stars.

We inspected the stacked, sky-subtracted frames from each of the four narrowband, multislit observations for emission lines. Line detection was then automated with SExtractor (version 2.3.2, Bertin & Arnouts 1996), requiring detection over at least 9-contiguous pixels, corresponding to a spatial width  $\geq 0''6$  and a line width  $\geq 6.4\text{\AA}$ . The SExtractor software recovered our initial, by-eye list of sources; additional candidates were inspected and found to be associated with incomplete masking of chip edges, zero-order images, and cosmic-rays. The SExtractor software worked well for finding the emission-line spectra because the signal from a line is very similar to that from an object in a direct image. The photometry from SExtractor is not appropriate for our survey however, because sky and continuum subtraction needed to be handled with techniques specific to spectroscopic data.

We measured the flux of each emission line in a fixed apertures using IRAF. This line photometry was performed on the images prior to sky subtraction using apertures defined on the sky-subtracted frames. Because faint,

sky lines are present even in this relatively clean window, care had to be taken to measure the average sky counts from exactly the same bandpass as the line aperture. Continuum was measured in the same spatial aperture as the line but was usually undetected. A flux calibration was derived from observations of spectrophotometric standards taken during each run. The throughput during the April 2004 run was 28% better than that during the spring 2005 runs due to a recent re-aluminization of the telescope mirror. The uncertainty in this calibration is 5-10% (except for the 2005 May search), and our photometric errors are normally dominated by the random pixel-to-pixel variations in the background under the object and/or the Poisson noise from the total counts. The May run was generally clear but not photometric, and we adopt the flux calibration derived 2 months earlier with the identical instrumental setup.

## 2.2. Broad Bandpass Spectroscopy

We obtained spectra of emission-line candidates with IMACS, a low resolution grism (usually  $200\text{ mm}^{-1}$ ), the GG455 blocking filter, and multislit masks with 1''5 slits. Masks for the 10H field were observed in 2005 May (4.5 hrs) and 2007 March (5.0 hrs). Masks in the 15H field were observed in 2004 July (7.0 hrs), 2005 June (2.0 hrs), and 2006 June (3.08 hrs with the  $150\text{ mm}^{-1}$  grism). The wavelength coverage for a typical source was 5500 Å to 9500 Å. The COSMOS<sup>4</sup> data reduction package was used to stack frames, remove cosmic rays, subtract sky, calibrate wavelength, and extract spectra. The 2007 March and 2004 July observations of the 10H and 15H fields, respectively, are significantly more sensitive than the other follow-up observations.

To date, low-resolution spectra have been attempted for 95% of the emission-line objects in both the 10H and 15H fields with a recovery rate of 80% and 95%, respectively. Relative astrometric errors were of particular concern for pre-corrector discoveries in the 2004 data, but we found no tendency for unrecovered objects to be on the periphery of the field.

## 2.3. Higher Resolution Spectroscopy

We obtained higher resolution spectra of Ly $\alpha$  candidates in the 10H Field with the IMACS long, f/4 camera and the  $1200\text{ mm}^{-1}$  grating in 2006 February. Line emission from sources filling the 1''5 slits has a FWHM of  $94\text{ km s}^{-1}$ ; and the resolution for unresolved objects is  $50$  to  $63\text{ km s}^{-1}$ . The two masks included only a subsample of the candidates passing the f/2 follow-up. Exposure times of 8.24 hrs and 8.75 hrs were sufficient under clear conditions to detect most targets. Some data for the 15H Field were obtained with the same configuration in 2006 February (6.0 hrs and some cloud cover) and 2006 June (3.5 hrs with cirrus; and 5.0 hrs under clear skies).

<sup>2</sup> The Perl Data Language (PDL) has been developed by K. Glazebrook, J. Brinchmann, J. Cerney, C. DeForest, D. Hunt, T. Jenness, T. Luka, R. Schwebel, and C. Soeller and provides a high-level numerical functionality in the perl scripting language (Glazebrook & Economou, 1997). It can be obtained from <http://pdl.perl.org>.

<sup>3</sup> The Image Reduction and Analysis Facility, a general purpose software system for the reduction and analysis of astronomical data. IRAF is written and supported by the National Optical Astronomy Observatories, which is operated by the Association of Universities for Research in Astronomy, Inc. under cooperative agreement with the National Science Foundation.

<sup>4</sup> The Carnegie Observatories System for MultiObject Spectroscopy was created by A. Oemler, K. Clardy, D. Kelson, and G. Walth; it is available at <http://www.ociw.edu/Code/cosmos>.

Resolved spectra in the 15H field were obtained at Keck in 2006 May using the  $831 \text{ mm}^{-1}$  grating on LRIS (Oke et al. 1995). Under thin clouds, integration times of 1.5 to 3 hrs yielded detections of most sources. Through the  $1''.5$  slits, telluric emission-lines had a FWHM of  $143 \text{ km s}^{-1}$ , and spectra of unresolved sources had spectral resolution of 76 to  $95 \text{ km s}^{-1}$ .

### 2.4. Continuum Imaging

Deep, broadband imaging complements our emission-line survey because it is more sensitive to continuum emission. Photometry can confirm redshifts via identification of the Lyman break, measure star formation rates via the strength of the rest-frame UV continuum, and constrain age via the Balmer break. Scattering of  $\text{Ly}\alpha$  photons by intergalactic hydrogen at  $4.0 < z < 5.7$  attenuates the continuum between the Lyman break and the  $\text{Ly}\alpha$  line, allowing only  $\sim 20\%$  transmission (Fan et al. 2002). At redshift 5.7, the  $\text{Ly}\alpha$  line falls in the  $i'$  (and  $i$  or  $I$ ) band, so imaging in  $z$  (or IR) filters provides UV (optical) continuum measurements. Much of the  $r'$  (and  $r$  and  $R$ ) bandpass lies below the Lyman limit. Only filters passing light shortward of the Lyman limit provide good veto imaging for high-redshift candidates.

#### 2.4.1. 10H Field

Taniguchi et al. 2007 present Subaru/Suprime-Cam imaging of the COSMOS field in the UBgVrIz broadbands and one narrowband NB816. The imaging redward of our emission lines reaches  $z' = 25.9$  (Taniguchi et al. 2007;  $2''$  diameter apertures;  $3\sigma$ ), which is deeper than the  $z \approx 25.0$  (S. Gwyn website)<sup>5</sup> imaging from the Canada France Hawaii Telescope Legacy Survey (CFHTLS-Field D2). Most of the emission-line objects that we find are not bright enough,  $\geq 5 \times 10^{-17} \text{ erg s}^{-1} \text{ cm}^{-2}$ , to be detected in the COSMOS  $z'$  band.

Assuming flat or redder SEDs (spectral energy distributions) in  $f_\nu$ , objects not detected in the Subaru  $z'$  imaging will not be detected in either the Subaru  $i'$  imaging or the HST ACS F814W observations. The latter are slightly more sensitive than the Subaru imaging for sources less than  $1''$  in diameter. The bandpass of our  $8190 \text{ \AA}$  filter lies just within the red limit of these filters, so these broadband filters sample mainly attenuated continuum. The  $Bg'V$  bands from COSMOS/Suprime-Cam are below the Lyman limit of  $z = 5.7$  objects, so a detection would veto identification of the object as a high-redshift galaxy.

#### 2.4.2. 15H Field

Far less imaging is available for the 15H Field. The  $z'$  imaging from LCIRS is significantly deeper than the infrared imaging. It reaches  $z' = 23.5$ , equivalent to  $z'_{AB} = 24.0$ .

We obtained a new, deep image in a  $3000 \text{ \AA}$  wide filter, WB48-78, in 2005 March. A total of 3.5 hr of integration was obtained with the IMACS short camera on Magellan. The blue half of this bandpass lies longward of the Lyman limit, but the red half includes the  $\text{Ly}\alpha$  and  $\text{Ly}\beta$  attenuated continuum. Null detections in the WB48-78 image

can therefore confirm a continuum break, but a detection does not necessarily rule out a continuum break.

## 3. RESULTS

### 3.1. Detection of Emission Lines

Over cosmological distances, the HI opacity of the IGM blankets the continuum from the Lyman limit to the  $\text{Ly}\alpha$  line, effectively shifting the continuum break up to the  $\text{Ly}\alpha$  line (Madau 1995). Any continuum blueward of a redshift 5.7  $\text{Ly}\alpha$  line must be weak due to  $\text{Ly}\alpha$  scattering along the line-of-sight. None of the line-plus-continuum spectra present continuum breaks across the emission line, so we excluded all the line-plus-continuum sources from the preliminary list of 136  $\text{Ly}\alpha$  candidates. Few of the line-only objects in the 10H field were detected in the Subaru narrowband image confirming our argument that spectroscopic surveys offer unique emission-line sensitivity. Table 2 shows the object yield for each of the four search runs, distinguishing line emitters with and without continuum in their discovery spectra.

### 3.2. Confirmed LAEs

We have confirmed three LAEs among the emission-line galaxies: MSDM80+3 in the COSMOS field and MSDM29.5+5 and MSDM71-5 in the 15H field. Confirmation requires: (1) the broad bandpass spectrum presents no spectral lines between  $\sim 5500$  and  $9500 \text{ \AA}$  other than the discovery line near  $8200 \text{ \AA}$  and (2) the profile of this line, at higher dispersion, is skewed to red wavelengths, consistent with transmission through high-redshift IGM. In this section, we present spectra of these three objects, put limits on the number of LAE candidates, and derive the survey completeness. Properties of the LAEs are further discussed in § 4.1.

Lyman-alpha-emitter MSDM29.5+5 from the 15H field shows the classic red-skewed line asymmetry of a LAE in the high-resolution, Keck spectrum; see panel (c) of Figure 3. The line width is  $235 \text{ km s}^{-1}$  FWHM. The low resolution spectrum, panels (a) and (b), is not sufficient to recognize the asymmetry. The line in the 200-l spectrum is narrower than the overlaid sky line, indicating a source size considerably smaller than the slit. The attenuated  $\text{Ly}\alpha$  flux is  $\sim 1.8 \pm 0.2 \times 10^{-17} \text{ erg s}^{-1} \text{ cm}^{-2}$  in the 2005 May discovery spectrum. The systematic errors in the flux calibration may be more uncertain than this statistical error due to the observing conditions described in § 2. The observed-frame equivalent width is at least  $11 \text{ \AA}$  based on the  $3\sigma$  upper limit on the continuum in the search spectrum. This object is outside the field of the LCIRS image.

Figure 4 shows LAE MSDM80+3, discovered in the 2004 search of the 10H field. The broad bandpass spectrum shows a slight red asymmetry of questionable significance. The higher resolution spectrum shows multiple line components spread over about  $400 \text{ km s}^{-1}$  FWHM. The  $\text{Ly}\alpha$  flux is  $1.4 \pm 0.2 \times 10^{-17} \text{ erg s}^{-1} \text{ cm}^{-2}$ . The  $3\sigma$  limiting  $z'$  flux (for  $2''$  diameter apertures) gives a lower limit on the observed-frame equivalent width of  $144 \text{ \AA}$ .

We believe MSDM80+3 is the same object as #55 detected by Muramyama et al. (2007) using

<sup>5</sup> <http://www3.cadc-ccda.hia-ihp.nrc-cnrc.gc.ca/community/cfhtls-sg/docs/cfhtls.html>

Subaru/Suprime-Cam narrowband imaging. The declinations agree to  $0''.2$ . Their right ascension is nearly  $1''0$  west of ours, consistent with the zeropoint shift we found relative to the Subaru image in § 2. They estimate a significantly higher line flux of  $2.8 \pm 0.4 \times 10^{-17}$  erg s $^{-1}$  cm $^{-2}$ . The discrepancy could result from attenuation of the source by our slit. Line fluxes from narrowband imaging are, however, subject to uncertainties about redshift, filter transmission, and continuum level. Since no continuum is detected from MSDM80+3 in broadband  $i'$  or  $z'$  images (Taniguchi et al. 2007) and we find a wavelength near the center of the filter bandpass, we see no obvious reason for the imaging result to be in error. We quantify our slit losses on a statistical basis in § 3.4 and include them in modeling the number counts in § 4.2.

Another line-emitter, MSDM71-5, marginally meets our criteria to be labeled “confirmed.” The shape of the line-profile leaves some ambiguity. Figure 5 shows follow-up spectra of MSDM71-5 taken with the 200-l and the 150-l grisms. Even at such low resolution, both of these spectra hint at a broad, red wing. Curiously, our high resolution Keck, LRIS spectrum shows a narrow line. It is highly unlikely that different objects were observed with the two telescopes because the line appears at the same wavelength in all 3 spectra. The B and z LCIRS images show no objects near the position of MSDM71-5. We detect an object slightly less than  $1''.5$  to the southeast in our deeper WB48-78 image; but, as explained in § 2.4.2, a weak detection in this band does not veto a line identification as Ly $\alpha$ .

The coordinates, approximate wavelength, and line flux of these confirmed LAEs are given in Table 3. We also tabulate the properties of emission line objects for which identification of the line as Ly $\alpha$  has not been ruled out, as we explain in the next section.

### 3.3. Additional LAEs?

We now ask whether our selection criteria may have missed some LAEs. Our follow-up observations were unusually complete. Low resolution, follow-up spectroscopy has been attempted for all but three *line-only* objects in each field. Should we have rejected all the *line-plus-continuum* objects? Many line-plus-continuum objects were in fact used to fill our follow-up masks. All their spectra obtained to date have been identified as foreground objects (see Table 2), so our initial continuum cut appears to be valid. The only sources that allow further speculation are the un-recovered targets and the galaxies that present a single emission line, i.e. just the discovery line near 8200Å, in their broad bandpass follow-up spectrum.

Table 2 reveals that in the 10H and 15H fields, 13 and 7 candidates, respectively, were not recovered by follow-up observations. Some candidates with line fluxes near the detection limit, derived in § 3.4, will inevitably turn out to be spurious. Review of the stacked, search data, led us to believe the majority of such sources were genuine, however. We attribute some failed recoveries, particularly for the 2004 sources, to the relative astrometric errors described in § 2.2. The fraction of LAEs among these objects is presumably as small as it is for the full sample, so we estimate 0 - 1 LAEs were missed. Our follow-up observations are also biased against detecting the faintest LAEs in our sample. Time and weather limitations resulted in

broad bandpass spectroscopy with half the exposure time of the initial search. These objects may include a higher, but unknown, fraction of LAEs.

Another set of 14 candidates (7 in the 10H field and 7 in the 15H field) are listed in Table 3. These objects present a single emission-line, at  $\sim 8200$  Å, in their broad bandpass spectrum. Higher resolution spectra, had they been obtained for these objects, would differentiate between LAEs, foreground [OII] emitters at  $z = 1.2$ , and extremely faint [OIII] 5007 emitters – i.e. those with undetectable [OIII] 4959 and H $\beta$  lines. Among the objects observed at higher-dispersion, the yield of LAEs to [OII] emitters varied widely among fields, making it difficult to predict the LAE fraction among the single-line sources. We gained additional insight from photometric redshifts from COSMOS (Mobasher et al. 2007) in our 10H field. The continuum emission from our candidates is typically fainter than the  $i' < 25$  completeness limit. We did investigate the redshifts of foreground galaxies near the sightline to each line emitter, however, with the idea that associated satellite galaxies or HII regions might be the source of the detected line emission. We find foreground galaxies surprisingly close to many of the single-emission-line galaxies, and their photometric redshifts often allow [OII] emission to be shifted into our search bandpass. For readers interested in the exact accounting, sections 3.3.1 and 3.3.2 review the single-emission-line objects individually in the 10H and 15H fields, respectively.

#### 3.3.1. Single-Emission-Line Candidates in the 10H Field

The low-resolution line profiles of the seven single-line candidates in the 10H Field are shown in Figure 6. The line profiles of MSDM52+8, MSDM17.5+8, and MSDM13-3 present significant skew. The spacing of the two peaks in the MSDM52+8 spectrum is consistent with [OII] emission; however, the bluer of the two emission peaks is stronger, which would imply a high electron density if the line is indeed [OII]. Electron densities in typical HII regions are lower than this, so this line can only be [OII] if it is an AGN (Active Galactic Nucleus), which will rarely be the case. In contrast, the profile shape of MSDM13-3 is consistent with a blended [OII] doublet in the low-density limit. These spectra lack the resolution required to reveal the asymmetry of many LAEs, such as MSDM29.5+5 in Figure 3, so a larger fraction of the single-line sources may actually have asymmetric line profiles.

To identify more interlopers, we searched the photometric redshift catalog of Mobasher et al. (2007) near the positions of our emission-line objects. The density of objects in the Subaru (UBgVrIz) imaging is such that a foreground galaxy brighter than the  $i=25$  detection limit lies within  $4''.5$  (or  $9''.0$ ) of a randomly chosen position 51% (or 92%) of the time. The projected distance to the nearest redshift 1.2, [OII]-emitting galaxy is larger. In the Mobasher et al. catalog, we find a galaxy consistent with being at redshift 1.2 within  $4''.5$  (or  $9''.0$ ) of a random sky position only 3.5% (or 11%) of the time. In light of these statistics, if the single-line objects are primarily LAEs, then very few (if any) will be projected near a galaxy with a photometric redshift near 1.2.

As expected, no foreground continuum sources are detected near our one confirmed LAE in the 10H field,

MSDM80+3. The closest galaxy whose photometric redshift is consistent with [OII] emission in our filter lies  $9''.9$  to the northeast. Our position for MSDM64-5 is  $2''.1$  northwest of the center of a foreground spiral galaxy with  $z_{\text{phot}} = 0.90$ . The 95% confidence interval,  $0.82 < z < 1.02$ , allows  $H\gamma$  (and plausibly a faint [OIII] 4363 line) to fall in our search band. The problem with this association is that  $H\beta$  and [OII] were not detected in the broad bandpass spectrum.

The other six single-line galaxies in the 10H field are likely foreground galaxies. All of them lie less than  $3''.5$  from a galaxy plausibly at redshift  $\sim 1.2$ . The associations are particularly close, in both angular separation and probable redshift, for MSDM30.5-8, MSDM17.5+8, and MSDM17-1. The separation is larger,  $2''.1$  (17.1 kpc at  $z = 1.2$ ), for MSDM52+8, but much of this discrepancy is in the direction of our astrometric (zero-point) error. We argued that MSDM13-3 is likely an [OII] emitter based on its line profile. Both MSDM13-3 and MSDM50-7 are very close to faint,  $i > 25$ , galaxies, which are known to be foreground owing to B-band detections. These offsets are small enough to be astrometric errors, and we tentatively assign our emission-line detection to the faint objects. These  $i > 25$  galaxies may be associated with the brighter, cataloged galaxies (near redshift 1.2) a few arcseconds away. Further work will be required to understand their physical nature.

### 3.3.2. Single-Emission-Line Candidates in the 15H Field

In addition to MSDM29.5+5 and MSDM71-5, we identified 7 single emission-line sources in the 15H field. Their  $f/2$  spectra are shown in Figure 7. The line profiles of MSDM57+4, and MSDM70+1 show some sign of asymmetry at low resolution. We interpret the blue skew of the MSDM70+1 profile as evidence of the [OII] doublet, an identification consistent with the source being the object in the (LCIRS) B band image, located less than  $1''.5$  from our estimated position. The only other single-line object with a B-band candidate this close to our position is MSDM89-2, which we also exclude from the candidate LAEs on the basis of a probable B-band detection.

All the single-line candidates show at least a faint smudge in the WB48-78 image within  $1''.5$  of our position. If these faint objects are the counterparts of our LAEs, they should be brighter in the  $z$  band. These galaxies are not detected in the LCIRS- $z$  images, but the depth is not sufficient to rule out a continuum break across the line. It is only the high frequency of plausible [OII] interlopers in the 10H field that strongly suggests many will turn out to be foreground interlopers. The extreme depth of the WB48-78 image does demonstrate that plausible continuum counterparts can be found at offsets from the emission-line objects that are significantly smaller than those from bright objects with photometric-redshifts in the 10H field. This result strengthens our suspicion that the objects near redshift 1.2 that are several arcseconds from our emission-line position are *not* the same source, although the two objects may be associated (i.e. at the same distance).

### 3.4. Completeness and Effective Area

To determine completeness levels, we added objects of various brightness to the search frames and then checked

whether SExtractor recovered them. The intensity of an object was modeled by a gaussian profile ranging in size from  $0''.45$  to  $0''.90$  spatially and linewidth  $6\text{\AA}$  to  $12\text{\AA}$ . We tuned SExtractor to find most of our by-eye sources but not to go too much fainter, which yields many spurious sources. This tuning requires that an object have at least 10 pixels above 1.5 times the background rms. SExtractor found 90% of our by-eye sources and most of the 'missing' 10% can be explained as being near image artifacts that confuse SExtractor. This tuning of SExtractor allowed us to recover the simulated sources in a way that was both automated and very close to what the human eye finds.

Results of the Monte Carlo simulations are shown in Figure 8. Most of our sources were unresolved spatially, so we interpolate to the results for  $0''.7$  seeing. The recovery rate of our survey is 50% at a line flux of  $6 \times 10^{-18} \text{ erg s}^{-1} \text{ cm}^{-2}$  for the most sensitive search, the 2004 observations of the 15H field, degrading to  $9 \times 10^{-18} \text{ erg s}^{-1} \text{ cm}^{-2}$  for the least sensitive search, the 2005 15H field.

Attenuation by the slit and masked areas such as chip edges, the zero-order image of the mask, and bright foreground objects affect the effective area of our survey. The Monte Carlo simulations quantify how the slit length that we can search is reduced by masked objects. For a fixed slit width of  $1''.5$ , this effective slit length per IMACS pointing ranged from  $45.134 \square'$  in the 15H 2005 search to  $45.589 \square'$  in the 10H 2005 search. The effective area over which a particular source could have been detected depends on its brightness. Emission-line objects near our detection threshold will only be detected if a slit is centered on them, while extremely bright sources could be highly attenuated and still detected. These slit losses were modeled using a Gaussian brightness profile as illustrated in Figure 9.

We modeled the effective slit length and completeness separately for each of our four search runs. The calculations in the next section use the results.

## 4. THE LAE GALAXY POPULATION

In this section, we discuss the properties of the LAEs, compute their space density, and find the families of Schechter function parameters that can describe this galaxy population. These descriptions of the LAE population are used to estimate the production rate of Lyman continuum photons, which is compared to the ionization requirement of the IGM at redshift 5.7.

### 4.1. Properties of LAEs

The  $\text{Ly}\alpha$  fluxes that we measured correspond to luminosities of  $\log \text{Ly}\alpha \text{ (erg s}^{-1}\text{)} = 42.70, 42.81, \text{ and } 42.89$  for MSDM80+3, MSDM29.5+5, and MSDM71-5, respectively. These LAEs are fainter than the luminosity break (i.e.  $L_*$ ) fitted to a larger sample of LAEs in the Subaru Deep Field (Shimasaku et al. 2006). Other surveys that have confirmed LAEs this faint at  $z \sim 5.7$  include: GRAPES – the Grism ACS Program for Extragalactic Science (Pirzkal et al. 2007) in the Hubble Ultra Deep Field (HUDF, Beckwith et al. 2006), the Gemini Deep Deep Survey (GDDS) – which obtained 30 hr spectroscopic observations of i-dropouts in the HUDF (Stanway et al. 2006), a survey of cluster caustics for lensed LAEs (Ellis et al. 2001), and the narrowband imaging surveys of Hu et al. (2004) and Shimasaku et al. (2006) with Subaru.

We estimate star formation rates for the Magellan LAEs from their line luminosities. Carrying the amount of Ly $\alpha$  attenuation,  $f_{ly\alpha}$ , along as a parameter, the Kennicutt (1998) conversion from H $\alpha$  luminosity to SFR and the Ly $\alpha$  to H $\alpha$  flux ratio from Case B recombination (Brocklehurst 1971) yield star-formation rate estimates

$$SFR = 1.0 f_{Ly\alpha}^{-1} M_{\odot} \text{ yr}^{-1} (L_{Ly\alpha} / 1.05 \times 10^{42} \text{ ergs s}^{-1}) \quad (1)$$

This expression assumes continuous star formation, solar metallicity, and a stellar initial mass function with  $d\log N/d\log M = -2.35$  from 0.1 to 100  $M_{\odot}$ . The estimated SFRs of the LAEs are  $4.8 f_{ly\alpha}^{-1}$ ,  $6.1 f_{ly\alpha}^{-1}$ , and  $7.4 f_{ly\alpha}^{-1} M_{\odot} \text{ yr}^{-1}$ . Variations in the ratio  $L(Ly\alpha)/L_{\nu}(UV)$  are large among LAEs, but star formation rates derived from the UV continuum are typically a factor of a few times higher than those estimated from Ly $\alpha$  (e.g. Pirzkal et al. 2007). The faint LAE population is very blue (Stanway et al. 2006; Pirzkal et al. 2007), so the upward corrections to these UV luminosities for extinction may be small. Our guess for the new LAEs is an attenuation  $f_{ly\alpha} \sim 0.25 - 0.5$ , which corresponds to SFRs of  $\sim 10 - 30 M_{\odot} \text{ yr}^{-1}$ .

Broadband photometry of the COSMOS field (and the LCIRS field) is not currently deep enough to detect the LAEs from the Magellan MNS survey. Rest-frame UV-to-optical colors are available for nine LAEs in the HUDF at slightly lower redshift  $4.0 < z < 5.7$ . Since the Ly $\alpha$  properties of the two samples are similar, the stellar masses estimated by Pirzkal et al. (2007) for the former,  $10^6$  to  $10^7 M_{\odot}$ , may be indicative of the masses of the Magellan MNS LAEs. The LAEs are not resolved in good seeing, so the size of the emitting region is less than about 5 kpc.

The shapes of the Ly $\alpha$  line profiles contain additional information about the properties of LAEs and the intervening IGM. Due to the high scattering cross section of the Ly $\alpha$  transition, modeling the diversity of Ly $\alpha$  profiles observed in star forming galaxies requires radiative transfer calculations (Ahn et al. 2003; Hansen & Oh 2006; Verhamme, Schaerer, and Maaselli 2006; Tapken et al. 2007). Outflows are thought to decrease the intrinsic Ly $\alpha$  attenuation via frequency shifting, so their presence may make it easier to detect Ly $\alpha$  emission. Since the Magellan LAEs have high SFRs, we interpret the line profiles in terms of the properties of galactic winds blown by the LAEs.

We measure Ly $\alpha$  linewidths of  $260 \text{ km s}^{-1}$  and  $240 \text{ km s}^{-1}$  FWHM, respectively, for MSDM80+3 and MSDM29.5+5. The Ly $\alpha$  line in the Keck spectrum of MSDM71-5 is only  $98 \text{ km s}^{-1}$  wide, but the line is broader in the low-resolution Magellan spectrum. We attribute the discrepancy to spatial variations across the object, which are weighted differently by seeing and slit alignment.<sup>6</sup> We fitted very simple single-component and two-component models to the high-resolution line profiles. The one component model is a Gaussian with all flux blueward of the peak set to zero to mimic absorption by intergalactic gas. This kernel was convolved with another Gaussian that represents the instrumental broadening. The 2-component model has an additional, weaker Gaussian added redward of the main line to simulate backscattering off an outflow.

The lower right panels of Figures 3, 4, and 5 show the results. The profile of MSDM29.5+5 is well fitted with

a single component. The fitted instrumental smoothing,  $\sim 110 \text{ km s}^{-1}$  FWHM, is consistent with the resolution of the Keck-LRIS, follow-up spectrum. The model indicates a FWHM prior to attenuation of  $400 \text{ km s}^{-1}$ . The high-resolution spectrum of MSDM80+3 shows a red wing. For an instrumental resolution of  $95 \text{ km s}^{-1}$ , the fitted single-component model has a width of  $300 \text{ km s}^{-1}$  prior to attenuation. A spectrum with higher signal-to-noise ratio is needed to determine the reality of additional line components, such as a possible narrow component located  $300 \text{ km s}^{-1}$  redward of the main line.

We fitted a model introduced by Dawson et al. (2002) and Hu et al. (2004) that is now in common use. Westra et al. (2005, 2006) fitted the model to two extremely luminous LAEs at  $z \sim 5.7$  from WFILAS. The two-component model for MSDM80+3 reminds one of their result for LAE S11.5236, which has a second peak offset  $400 \text{ km s}^{-1}$  redward of Ly $\alpha$  that is only  $20\text{-}90 \text{ km s}^{-1}$  wide. This model has also been fitted to the composite line profile of LAEs discovered serendipitously in the DEEP2 redshift survey (Sawicki et al. 2007). The intrinsic width of the primary component  $\sim 350 \text{ km s}^{-1}$ , and the component fitted to the red wing is offset  $\sim 420 \text{ km s}^{-1}$ . These values are similar to what we find for the Magellan LAEs even though the DEEP2 LAEs are more luminous (mean  $L_{Ly\alpha} = 6 \times 10^{42} \text{ erg s}^{-1}$ ) and found at lower redshift (median redshift 4.1). The substantial star formation rates suggest that winds are the likely source of the redshifted emission, but gas inflow can produce similar line profiles (Dijkstra et al. 2006). Strong winds would play a critical role facilitating the escape of ionizing photons (Fujita et al. 2003).

#### 4.2. Number of LAEs Detected

We confirm three LAEs from the four survey masks. The total unobscured slit area and the filter bandpass at FWHM sample a volume of  $4.50 \times 10^4 h_{70}^{-3} \text{ Mpc}^3$ . The slit and the filter attenuate every LAE. The amount of attenuation is unknown for any individual source but is well understood statistically for the population. For any model of the luminosity function, we can accurately predict the attenuation of objects drawn from such a population and compute the number of sources detected given the completeness limit of each of our four search observations.

For parameterizations of the luminosity function ( $L_*$ ,  $\phi_*$ ,  $\alpha$ ), where

$$d\phi(L) = \phi_*(L/L_*)^{\alpha} e^{-L/L_*} d(L/L_*), \quad (2)$$

we computed the mean number of LAEs that our survey would detect. We calculated the volume from which a source is drawn using the slit width and redshift interval over which the source could have been detected. Because we start with the intrinsic luminosity (or flux), we can model the mean attenuation precisely. We discuss the results obtained using our 90% completeness level.

Figure 10 illustrates the range of luminosity function parameters that yield  $\sim 3$  detections. The shaded regions in Figure 10 denote the allowed combinations of  $(\phi_*, L_*)$  by requiring that the model yield 1.37 to 5.92 LAEs (85% confidence limits, orange) or  $3_{-2.18}^{+4.75}$  LAEs (95% CL in yel-

<sup>6</sup> The same object is detected by both observations because independent wavelength calibrations put the line at the same wavelength in both spectra.

low), where the limits were computed from Poisson statistics (Gehrels 1986). The number density of LAEs in the Magellan MNS survey constrains the product  $L_*\phi_*$  well. The contours of equal number show how lower normalization values,  $\phi_*$ , require higher  $L_*$  to yield a fixed number of objects  $N$ . Since our data do not constrain the faint-end slope well, we show results for three assumptions  $\alpha = -1.2, -1.6,$  and  $-2.0$ . In the limit  $\alpha = -2.0$ , a normalization similar to that at  $z \sim 4.9$  in the SDF,  $\phi_* \approx 0.0055 \text{ Mpc}^{-3}$  (Ouchi et al. 2003) requires  $L_*$  lie in the range  $1.78 \times 10^{42}$  to  $5.97 \times 10^{42} \text{ ergs s}^{-1}$ . As the faint-end slope becomes flatter, the characteristic luminosity must increase to yield 3 detected objects if the normalization is held fixed.

Based on our confirmation rate to date, additional spectroscopic follow-up will confirm, at most, a couple more LAEs in our emission-line survey. The number of remaining line sources for which a LAE identity has not been ruled out provides a strict upper limit. Our follow-up observations were remarkably complete; only 4 objects in the 10H field, and 7 candidates in the 15H field, were not re-observed without the blocking filter. Some emission-line objects, however, were not-recovered in follow-up spectroscopy (8 and 7 galaxies in the 10H and 15H fields, respectively). In the previous section, we argued that only two single-line objects in the 10H field were not likely foreground emitters. To compute an upper limit, however, we count all 9 single-line sources (including the confirmed LAE MSDM80+3). We found 7 single-line objects including 2 confirmed LAEs in the 15H field. The total number of remaining LAE candidates is 42. For comparison, adopting the Shimasaku et al. luminosity functions with  $\alpha = -2.0, -1.5,$  and  $-1.0$  yields 17, 14, and 12 LAEs, respectively, in our IMACS-MNS survey. That our upper limit is well above this confirms that most of our emission line objects that remain unidentified are not LAEs as we have argued.

#### 4.3. Cumulative LAE Luminosity Distribution

Monte Carlo simulations of the luminosity distribution are the preferred method for determining the best luminosity function parameters. For a larger (or deeper) survey with more sources than our survey, we would estimate the luminosity function parameters by drawing sources randomly from a model of the luminosity function, assigning them random positions in the field and applying the detection biases associated with the slit, filter, and data processing unique to MNS. The likelihood of the true parameters lying in any particular range could then be determined.

With just three confirmed LAEs, however, we use a simple variant of the  $1/V_{max}$  method (Felten 1976; Dawson et al. 2007) to estimate the cumulative luminosity distribution. We model the maximum volume,  $V_{max,i}$ , within which each source could have been recovered. We use the slit width and redshift interval within which the object would have a flux greater than that of our survey's 90% completeness limit. Due to the high fraction of candidates followed up and recovered, the correction for unobserved candidates is small and omitted. Proceeding from the brightest source to the faintest, we add up the number density of LAEs to obtain the cumulative luminosity distribution. Our best estimate is a lower bound in some

sense because of the possible attenuation of each LAE. Table 4 shows this cumulative luminosity function.

Figure 11 compares this distribution (solid squares) to counts from other surveys at redshift 5.7. The open squares denote faint LAEs from Santos et al. (2004) that are gravitationally lensed by a foreground galaxy cluster. This ground-breaking survey of cluster caustics demonstrates the existence of less luminous LAEs; but the LAE number density is far more uncertain than the statistical error (shown). The survey volume is difficult to estimate and very small (i.e. subject to cosmic variance), so one may not wish to weight these points heavily when constraining the luminosity function. The GRAPES produced three LAEs at  $z > 5$ ; the density from Pirzkal et al. (2007), which includes lower redshift LAEs, is denoted by a cross in Figure 11. The luminosities and redshifts of the LAEs discovered by Hu et al. (2004, open circles) with wide-field narrowband imaging provide the most direct comparison to our Magellan survey. The latter, like many of the imaging surveys, was carried out with the SuprimeCam mosaic CCD camera on Subaru but is unique among them; a high percentage of candidates have been confirmed spectroscopically. The number density of LAEs estimated from our Magellan MNS survey agrees very well with the result from the survey of Hu et al., which sampled a volume comparable to Shimasaku et al.

Number density estimates from the Large Area Lyman-Alpha survey still require significant extrapolation for unconfirmed LAEs at redshift 5.7 (Rhoads et al. 2001). Their best estimate (Malhotra & Rhoads 2004, open triangle) is, however, consistent with our new result. The data at redshift 5.7 will improve with the spectroscopic confirmation of other large surveys with SuprimeCam (Murayama et al. 2007; Ajiki et al. 2003, 2004, 2006). In Figure 11, we show LAEs, selected photometrically from SuprimeCam imaging of the Subaru Deep Field (SDF); Shimasaku et al. (2006) published spectroscopy for about one-third of the sample. For a faint-end powerlaw slope of  $\alpha = -2.0$ , their fitted characteristic luminosity is  $L_* = 1.6_{-0.6}^{+0.9} \times 10^{43} \text{ ergs s}^{-1}$  with normalization  $\phi_* = 1.6_{-0.7}^{+1.4} \times 10^{-4} \text{ Mpc}^{-3}$ ; and the integral of this luminosity function is plotted in Figure 12. The LAE number density of the Shimasaku et al. LAEs is 3-6 times higher than our result over the luminosity range  $\log L = 42.8_{-0.1}^{+0.1}$ . Inspection of the error bars in Figure 11 shows that only at the low end of this range are our results even marginally consistent.

It is not obvious to us that cosmic variance is the explanation of this discrepancy. Stark, Loeb, & Ellis (2007) argue quantitatively that the variance in the Subaru Deep Field LAE Survey at redshift 5.7 is dominated by Poisson shot noise rather than cosmic variance. The area imaged, about 0.20 square degrees, is similar to that covered by both the LALA survey and Hu et al. (2004). The shallow narrowband imaging survey, WFILAS (Westra et al. 2006), covers a larger area. Only two of 7 LAE candidates have been confirmed in their 0.72 sq. degree field, but these two objects are very luminous; and we show their number density in Figure 11 (hexagon). To estimate the total variance in our survey, we used the on-line calculator described by Trenti & Stiavelli (2008). To simulate the effect of the sparse sampling of the slits, we used a low value

for the survey completeness (10%) and the combined survey areas in the 10H and 15H fields. For any halo filling fraction less than 70%, the total variance was dominated by the Poisson term rather than the clustering term. We conclude that cosmic variance is unlikely to dominate the uncertainty in our measurement of the LAE number density.

The Shimasaku et al. result in the SDF is consistent with the WFLAS result considering their uncertainties, but the estimated values differ by a factor of five. Since several of these surveys probed large volumes, we see no reason to favor the newer Shimasaku et al. result until spectroscopic confirmation is completed. The combined data do not constrain the break luminosity,  $L_*$ , well in Figure 11.

#### 4.4. The Ly $\alpha$ Escape Fraction

The luminosity distribution of i-dropouts has been measured to very faint limits in the HUDF and a few other fields with deep HST/ACS observations (Bouwens et al. 2007; Bouwens et al. 2006). Since we do not detect continuum from our faintest LAEs, and spectra have not been acquired for all of the i-dropouts, it remains unclear whether the Ly $\alpha$ -selected sample is drawn from the i-dropout population. For purposes of illustration, we mapped the rest-frame UV luminosities,  $L_\nu$ , of objects drawn from the i-dropout luminosity function into line emission. We used the relation  $L(\text{Ly}\alpha) = 1.47 \times 10^{42} \text{ erg s}^{-1} f_{\text{Ly}\alpha} (L_\nu/10^{28} \text{ erg s}^{-1} \text{ Hz}^{-1})$ , which assumes a timescale for star formation inherent to the mapping from UV luminosity to SFR given by Kennicutt (1998). Figure 12 shows the cumulative Ly $\alpha$  luminosity function of the i-dropouts. The three models are labeled by the Ly $\alpha$  attenuation,  $f_{\text{Ly}\alpha}$ . For the no attenuation example, this heuristic model overpredicts the number density of LAEs.

The surprise is how easy it is to reconcile the number density of LAEs and i-dropouts. Absorption by intergalactic gas significantly attenuates the Ly $\alpha$  emission from  $z > 4$  galaxies. For redshift  $\sim 6$  galaxies, the SFR inferred from the UV luminosity is typically several times higher than that inferred from the Ly $\alpha$  luminosity. The dashed curves in Figure 12 show that absorbing the blue half of the line profile, equivalent to setting  $f_{\text{Ly}\alpha} = 0.5$ , is one way to produce the LAE luminosity distribution from the i-dropout population. This particular model is not unique and may be a strong oversimplification of the relation between these two galaxy populations. The ratio of UV to Ly $\alpha$  luminosity presents enormous scatter among galaxies. The escape fraction  $f_{\text{Ly}\alpha}$  could vary strongly with luminosity (or halo mass).

Additionally, if the fraction of galaxies presenting Ly $\alpha$  emission is less than unity, then the i-dropout luminosity function would need to be shifted in number besides star formation rate in order to model the LAE luminosity function. We know that only 25% of redshift 3 LBGs are LAEs (Shapley et al. 2003). The data for  $z \sim 6$  galaxy samples appear to disagree. Shimasaku et al. (2006) and Kashikawa et al. (2006) argue for a rise in the fraction of galaxies with Ly $\alpha$  emission to near unity at  $z \sim 6$ , while Dow-Hygelund et al. (2007) found many i-dropout galaxies without Ly $\alpha$  emission. Modeling the effect of color cuts and equivalent width cuts on these samples will be required

to clarify the Ly $\alpha$  emission fraction. The correct physical mapping between the i-dropout and LAE populations is not currently known. Our comparison simply shows that a simple model with 50% Ly $\alpha$  attenuation and a high fraction of LAEs among i-dropout galaxies is consistent with our estimated density of LAEs. That it severely overpredicts the counts from the lensed observations could mean a number of things: smaller Ly $\alpha$  escape fractions from dwarfs, an overestimate of the number of faint i-dropouts, or an underestimate of the number density of lensed LAEs.

#### 4.5. Reionization Constraints

The presence of Gunn-Peterson troughs in the spectra of  $z \sim 6$  quasars (Becker et al. 2001; Djorgovski et al. 2001) requires only a tiny neutral gas fraction in the IGM, about one in  $10^4$  H atoms. The absence of strong evolution in the shape of the LAE luminosity function between redshift 5.7 and 6.5 suggests little change in the neutral fraction leading many to believe reionization was complete by redshift 6.5 (Malhotra & Rhoads 2004; cf. Kashikawa et al. 2006). A protracted period of reionization from redshift 14 to 7 would be consistent with the Thompson optical depth inferred from measurements of the cosmic microwave background (Spergel et al. 2007). The time from redshift 7 to 5.7 is 229 Myr, long enough that the intergalactic gas would recombine were it not bathed with Lyman continuum radiation.<sup>7</sup> We therefore ask whether the LAE galaxy population discovered to date might supply these ionizing photons.

To maintain IGM ionization at  $z = 5.7$ , the number of ionizing photons escaping from galaxies over the recombination timescale must equal or exceed the number of hydrogen atoms. The recombination rate is faster in denser regions of the IGM, so the required number of escaping photons increases with the clumpiness of the gas. The gas is smoothest on large scales and clumpier in the virialized regions where galaxies form. The gas in these halos absorbs a high fraction of the ionizing photons (produced by galaxies), so the Lyman continuum escape fraction,  $f_{\text{Ly}C}$ , is lower on the larger scale of the IGM. For the regions of IGM penetrated by ionizing radiation, a clumping factor can be calculated that is the reciprocal of the volume filling factor of protons (or electrons). The clumping factor is defined here in units of  $C \equiv \langle n_{\text{HII}}^2 \rangle / \bar{n}_{\text{HII}}^2$  (Madau et al. 1999); and at  $z \sim 6$  it is likely between 1 and 10 (Furlanetto et al. 2006; Gnedin 2007). We parameterize the clumping factor in units of  $C = 6$  such that  $C_6 \equiv (1/6) \langle n_{\text{HII}}^2 \rangle / \bar{n}_{\text{HII}}^2$ . Following Madau et al. (1999), the critical ionization rate in the IGM is  $\dot{N}_H = \bar{n}_H(0)/\bar{t}_{\text{rec}}(z)$  per unit comoving volume, which we can write as

$$\dot{N}_H = 5.2 \times 10^{50} \text{ s}^{-1} \text{ Mpc}^{-3} C_6 \left( \frac{1+z}{6.7} \right)^3 \left( \frac{\Omega_b h_{70}^2}{0.047} \right)^2. \quad (3)$$

The required production rate of H ionizing photons in galaxies is much higher because little Lyman continuum radiation escapes (Hurwitz et al. 1997; Leitherer et al. 1995). Measurements at redshift 3 suggest absolute escape fractions  $f_{\text{Ly}C} \lesssim 0.1$  (Chen et al. 2007; Shapley et al. 2006; Inoue et al. 2005; Fernandez-Soto et al. 2003; Gial-

<sup>7</sup> The recombination time depends on the clumping factor of the IGM. Following Madau et al. (1995),  $t_{\text{rec}} = 290 \text{ Myr} C_6^{-1} \left( \frac{6.7}{1+z} \right)^3 \left( \frac{0.047}{\Omega_b h_{70}^2} \right)$ .

longo et al. 2002; Steidel et al. 2001). Numerical simulations suggest escape from the virialized halos of low mass galaxies is difficult (Gnedin et al. 2007) and that the result is sensitive to the interplay between the blowout of a galactic wind and the star formation history (Fujita et al. 2003). In the absence of any contribution from quasars, the minimum cosmic star formation rate<sup>8</sup> required to keep the universe ionized at  $z=5.7$  is

$$\dot{\rho}_* = 0.02 \text{ M}_\odot \text{ yr}^{-1} \text{ Mpc}^{-3} \times C_6 f_{LyC,0.1}^{-1} \left( \frac{1+z}{6.7} \right)^3 \left( \frac{\Omega_b h_{70}^2}{0.047} \right)^2, \quad (4)$$

where  $f_{LyC}$  is the fraction of Lyman continuum photons escaping from galaxies, and  $f_{LyC,0.1}$  means  $(f_{LyC}/0.1)$ . The ratio  $C/f_{LyC}$  is not very sensitive to spatial scale, so the spatial dependencies of the clumping factor and escape fraction cancel each other out to some extent.

To determine what fraction of this ionization requirement the source population provides, we can add up all the LAEs, weighting by luminosity, in a given volume of space. Using Case B recombination conditions and Equation 3, we find the critical Ly $\alpha$  luminosity density required for full IGM ionization is

$$L_{Ly\alpha} = 3.0 \times 10^{40} \text{ erg s}^{-1} \text{ Mpc}^{-3} \times C_6 (1 - 0.1 f_{LyC,0.1}) \left( \frac{f_{Ly\alpha,0.5}}{f_{LyC,0.1}} \right) \left( \frac{1+z}{6.7} \right)^3 \left( \frac{\Omega_b h_{70}^2}{0.047} \right)^2. \quad (5)$$

This equation highlights some obvious facts. If Ly $\alpha$  radiation is highly attenuated (i.e.  $f_{Ly\alpha} \ll 1$ ), then the observed Ly $\alpha$  luminosity density can be low even though the observed galaxy population ionizes the IGM. Likewise, if Lyman continuum leakage from galaxies is very low (i.e.  $f_{LyC} \ll 1$ ), then even a high number density of galaxies will not completely ionize the IGM. To visualize the implications of the uncertain gas physics for the IGM ionization requirement, we collect all the factors in Equation 5 describing the gas physics into a single parameter

$$\zeta = C_6 (1 - 0.1 f_{LyC,0.1}) f_{Ly\alpha,0.5} f_{LyC,0.1}^{-1}, \quad (6)$$

which is likely between 0.1 and 2. Although our simple modeling does not include possible variations in  $\zeta$  among galaxies, we note that our survey limit is brighter than that expected at the theoretical mass cut-off for escape of Lyman continuum photons (Gnedin et al. 2007; Gnedin 2007).

We consider the luminosity density of the LAE population for two minimum luminosities: the Magellan MNS detection limit of  $\log L_{Ly\alpha}(\text{erg s}^{-1}) = 42.57$  and an extrapolation to  $\log L_{Ly\alpha}(\text{erg s}^{-1}) = 41.0$ . This lower value corresponds to a  $SFR \approx 0.1 \text{ M}_\odot \text{ yr}^{-1}$ , a level of activity common among dwarf starburst galaxies at low redshift. The line flux of such objects,  $F_{Ly\alpha} \approx 3 \times 10^{-19} \text{ erg s}^{-1} \text{ cm}^{-2}$  at redshift 5.7, is well below current detection limits. For each luminosity function represented by the grid of Schechter function parameters in Figure 10, we integrated the Ly $\alpha$  luminosity density down to the two minimum luminosities. The total luminosity densities are shown in Figure 13. Only those values within the (orange and yellow) shaded region can be attained by a LAE population consistent with our number counts.

The Ly $\alpha$  luminosity density in Figure 13 is shown relative to that required for IGM ionization by Eqn. 5. Contours of equal luminosity density are labeled by the value of  $\zeta$  required for ionization; blue and red contours correspond to a minimum luminosity  $\min \log L_{Ly\alpha}(\text{erg/s}) = 42.57$  and 41.0, respectively, for the lower integration limit. If spatial variations in  $C_6$  and  $f_{LyC,0.1}$  do largely cancel out, then  $\zeta$  largely reflects the amount of Ly $\alpha$  attenuation,  $f_{Ly\alpha,0.5}$ . We consider values of  $\zeta$  from 0.1 to 2.0 to be plausible. Comparison of the blue contours to the allowed (i.e. shaded) region shows that the detected population of LAEs can only ionize the IGM if  $\log L_{*,Ly\alpha}(\text{erg s}^{-1}) < 42.4$ . Following the arguments of § 4.4, the luminosity break for the i-dropouts,  $M_{*,1600}$ , maps to  $\log L_{*,Ly\alpha} = 42.60$  for  $f_{Ly\alpha} = 0.5$ . Most previous Ly $\alpha$  studies have claimed  $L_{*,Ly\alpha}$  greater than 42.4 (Shimasaku et al. 2006; Malhotra & Rhoads 2004).

For a population of LAEs with  $\log L_{*,Ly\alpha}(\text{erg s}^{-1}) \gtrsim 42.5$  to ionize the IGM, galaxies much fainter than our detection limit must contribute to the ionizing radiation at  $z \sim 6$ . The blue contours do not intersect the allowed region in Figure 13 for high values of  $\log L_{*,Ly\alpha}$ . Extending the luminosity function to very faint limits helps produce the stellar mass that appears to have been assembled by  $z \sim 5$  (Stark et al. 2007a). The flatter the faint-end slope of the LAE population, the harder it becomes to ionize the IGM when  $L_{*,Ly\alpha}$  is high. When  $\log L_{*,Ly\alpha}$  increases much beyond 42.5 in Figure 13, the allowed (shaded) region is intersected only by the red contours with low values of  $\zeta$ . For large values of  $\log L_{*,Ly\alpha}(\text{erg s}^{-1}) \approx 43$ , the parameter  $\zeta$  must be  $\lesssim 0.1$  for complete ionization, much less if the faint-end slope is not steep. In our simple model, when  $\log L_{*,Ly\alpha}$  approaches 43, it becomes difficult for galaxies to ionize the IGM.

A galaxy population described by lower values of  $L_{*,Ly\alpha}$ , however, easily ionizes the IGM. In Figure 13, the intersection of the blue contours with the shaded region indicates normalizations  $\log \phi_{*,Ly\alpha}(\text{Mpc}^{-3})$  greater than -2.2, -2.25, or -2.37 are required for faint-end slopes  $\alpha = -2.0, -1.6, \text{ or } -1.2$ , respectively. These high normalization models pull the luminosity break down to  $\log L_{*,Ly\alpha}(\text{erg s}^{-1}) = 42.42, 42.38, \text{ and } 42.35$ , respectively. These values of the break luminosity are below the detection limit of the Magellan MNS survey, so the models produce a larger Ly $\alpha$  luminosity density per number of galaxies detected. If one accepts values of  $\zeta$  as low as 0.1, then even the galaxy population detected by our Magellan MNS survey can keep the IGM ionized at  $z = 5.7$ .

The volume of the Magellan MNS survey is not large enough to constrain  $L_*$  well. One could as easily fit our points in Figure 11 with a power law instead of a Schechter function. To our surprise, however, we found that the other LAE surveys do not appear to constrain  $L_*$  all that well. At redshift 5.7, a straight line can be drawn through the luminosity function data and error bars in Figure 1 of Malhotra & Rhoads (2004), particularly when the number densities from lensing are excluded. The fitted distribution is better constrained in Figure 11 of Shimasaku et al. , but considerable leeway remains due to poor constraints at the bright end. We looked to lower redshift surveys for LAEs

<sup>8</sup> Here, we have used an initial stellar mass function  $dN/dM \propto M^{-2.35}$  from  $1.0 \text{ M}_\odot$  to  $100 \text{ M}_\odot$ . Continuous star formation at a rate of  $1.0 \text{ M}_\odot \text{ yr}^{-1}$  produces ionizing photons at a rate of  $\dot{N}_H = 10^{53.4} \text{ s}^{-1}$  (Kennicutt 1998; Leitherer et al. 1999).

to determine what values of  $L_*$  might be reasonable. The MUSYC survey at  $z \sim 3$ , in fact, favors significantly lower values,  $\log L_{*,Ly\alpha}(\text{erg s}^{-1}) = 42.64^{+0.26}_{-0.15}$  (Gronwall et al. 2007); but inspection of their Figures 10 and 11 suggests the luminosity break is again not that well constrained due to the relatively shallow survey depth. It is possible that  $L_{*,Ly\alpha}$  is lower at  $z = 5.7$  than at redshift 3 since  $M_{UV}^*$  may fade with lookback time from redshift 4 to 6 (see Bouwens et al. 2007; cf. Iwata et al. 2007).

We question whether these lower  $L_{*,Ly\alpha}$  models have been ruled out by the data at this time. If not, then the population of LAEs detected could contribute a high fraction of the radiation needed to maintain the ionization of the IGM at redshift 5.7. If  $L_{*,Ly\alpha}$  is large, then a large extrapolation of the luminosity function to fainter sources is required for LAEs to account for the ionizing photons. The faintest  $z = 5.7$  galaxies recovered by the lensing surveys have unlensed luminosities of  $\log L_{Ly\alpha} \sim 41.4$ , a factor of 2.5 higher than the value of  $L_{min}$  used to compute Figure 13. Although there is tentative evidence for a steep faint-end slope (Stark et al. 2007b; Kashikawa et al. 2006), it seems likely that new technology will be required to determine definitively whether star-forming galaxies ionize the IGM at high redshift.

## 5. EMISSION-LINE DETECTION OF HIGH-REDSHIFT GALAXIES

We have demonstrated that multislit, narrowband spectroscopy is a viable technique for finding LAEs at redshift 5.7. Here we compare the efficiency of this sky-suppression technique to other strategies using current instrumentation. The sensitivity limits of next generation facilities to emission-lines are then discussed. Hydrogen Ly $\alpha$  emission will be the brightest line where the local gas kinematics allow escape and the IGM neutral fraction allows significant transmission. Our discussion focuses on Ly $\alpha$  detection over the period of reionization from  $6 < z < 30$  but also applies to nearby lines like HeII 1640, CIV 1550, and NV 1240.

The canonical figure-of-merit for galaxy surveys is the product  $A\Omega$ , where  $A$  is the collecting area of the telescope and  $\Omega$  is the solid angle of sky observed at one time. The time required to survey a given area of sky to a particular magnitude is then inversely proportional to  $A\Omega$  for broadband imaging. For emission-line surveys, the quantity to maximize, when sky emission is the dominant source of noise, is  $A\Omega\epsilon/(\Sigma_\lambda\Delta\lambda\theta^2)$ , where  $\Delta\lambda$ ,  $\theta^2$ , and  $\epsilon$  represent spectral resolution, image size, and system throughput, respectively. For Ly $\alpha$  observations from redshift 4 to 20 ( $\lambda_0 = 0.6 - 2.6\mu\text{m}$ ), the surface brightness of the sky,  $\Sigma_\lambda$  is dominated by the zodiacal background in space. Its brightness is a strong function of distance from the ecliptic plane and was measured with COBE (Hauser et al. 1998; Kelsall et al. 1998). Atmospheric bands of molecular lines, mainly OH (hydroxyl and  $O_2$ ), dominate the broadband background from the ground. The interline background at high-dispersion is much lower than the broadband mean, but its physical origin and intensity are not well understood. Maihara et al. (1993) suggest it is a few times brighter than the zodiacal background, but Bland-Hawthorne et al. (2004) argue that most of this emission is scattering and diffraction of the molecular lines. Here, we

will assume the standard interline background from Maihara, and explore how the spectral resolution, image quality, and system throughput inherent to various observing techniques affects both sensitivity and survey efficiency.

Due to the high number of interlopers in many surveys for galaxies across the reionization era, this revised figure-of-merit does not completely describe the potential impact of a survey. The time required for redshift confirmation, not just that used to identify candidates must be considered. In this regard, emission-line *sensitivity* is also of relevance for surveys employing continuum-break selection.

### 5.1. Current Capabilities for Detecting Faint, Emission-Line Galaxies

Emission-line spectroscopy with large, ground-based telescopes offers high sensitivity to objects with low SFRs. The HUDF observations with HST/ACS reached an exceptional broadband depth. The luminosity function of *i*-dropouts reaches  $M_{UV,AB} = -17.5$  (Bouwens et al. 2007), a star formation rate of  $0.6 M_\odot \text{ yr}^{-1}$ . The Ly $\alpha$  emission from a subsample of these galaxies was detected in 30 hr integrations with Gemini (Stanway et al. 2006). Fainter LAEs clearly exist as shown by their detection with gravitational lenses (Ellis et al. 2001; Santos et al. 2004).

Here we compare current capabilities of MNS, NB imaging, and tunable filters. Our arguments about the benefits of spectroscopy apply equally to observations with integral field units. The small fields of view of IFUs are inefficient for surveys at redshifts where the neutral fraction is low. At  $z \sim 10$ , however, the only detectable LAEs may be those within the ionized bubbles of the brightest sources. Furlanetto & Oh (2005) estimate physical sizes of 27 to 227 kpc. Band-limited IFUs with diameters of 6-60" would be extremely effective for studying these galaxies. Slitless grism spectroscopy is never more sensitive than NB imaging because each pixel records background from the full transmitted bandpass. It has been used effectively from space owing to the lower background there and the benefits of low resolution spectra for identifying very faint galaxies (Xu et al. 2007; Pirzkal et al. 2007).

#### 5.1.1. Narrowband Imaging vs. Spectroscopy

For any telescope and instrument for which emission-line detection is sky-noise limited, let us compare surveys carried out with MNS to those done with narrowband imaging. In a fixed amount of integration time  $t$ , spectroscopic observations detect fainter emission lines because the bandpass of sky under the line,  $\Delta\lambda$ , is typically much less than the width of the filter,  $\Delta\lambda_0$ . Maximum depth results from matching the spectroscopic resolution to the Ly $\alpha$  linewidth. For a representative width of  $150 \text{ km s}^{-1}$ , the factor  $\Delta\lambda/\Delta\lambda_0$  is approximately  $4.1\text{\AA}/150\text{\AA} \approx 6^{-2}$ ; and the line flux reached with MNS is

$$F = F_0 \sqrt{\frac{\epsilon_0}{\epsilon} \frac{\Delta\lambda}{\Delta\lambda_0} \frac{\theta}{\theta_0} \frac{t_0}{t}}, \quad (7)$$

where quantities denoted by subscript zero represent narrowband imaging. Our IMACS pilot survey carried out with the facility 200-l grism collected a  $6.4 - 12.8\text{\AA}$  band of sky under each emission line, so it did not reach maximum depth. Many emission-line sources were unresolved by our observations, setting an upper limit on their size of

$\theta \lesssim 0''.75$  FWHM. Better image quality would reduce sky noise further for both imaging and spectroscopy. The factor of  $\sqrt{\theta(\text{slit})/\theta_0}$  in Eqn. 7 equals  $\sqrt{1.5/\theta_0}$  for our pilot survey. The gain appears larger for imaging because the sky aperture for MNS is fixed by the slit width in one spatial dimension, yielding a linear rather than a quadratic decrease in sky photons with seeing. For our pilot survey, we cut slits twice as wide as the seeing to mitigate attenuation by the aperture. Hence, we think  $\sqrt{\theta/\theta_0}$  can be tuned to a factor  $\sim \sqrt{2}$  in any seeing. The penalty in throughput,  $\epsilon$ , from the addition of the dispersing element is minor; for the 200-l grism, the relative sensitivity is reduced by just  $\epsilon/\epsilon_0 \sim 0.89^2$ . We conclude that had we used our telescope time for NB imaging, our flux limit would be a factor of 3.0 to 4.3 times higher (i.e. less sensitive).

When the total time required to search a given volume of space for emission-line sources is considered, the gain in sensitivity from MNS, relative to NB imaging, is offset by the lower solid angle (per pointing) of the former. With the 200-l grism, the clear aperture of the IMACS-MNS experiment subtends  $55.3/656 = 8.4\%$  of the active imaging field. In the time required to observe 12 masks, the integration time for direct narrowband imaging of a single field could be increased to  $t_0 = 12t$ , increasing the line sensitivity to match that of MNS with IMACS. Narrowband imaging and MNS therefore reach comparable emission-line sensitivity when normalized by the volume searched per unit observing time. It is easy to show that this equivalence continues to hold as spectral resolution increases.<sup>9</sup> In a given amount of time, MNS reaches considerably fainter lines than NB imaging but selects from a smaller volume. When the objective is to optimize the yield of the faintest sources, the MNS technique is a better choice than NB imaging.

The development of MNS will allow more sensitive surveys in the 8200Å atmospheric window. Detector quantum efficiency, grism blaze, and spectral resolution can all be improved for IMACS observations, but installation of the new E2V CCDs will provide the single largest gain in throughput. In a deep  $\sim 25$  hr survey, we expect to reach a line luminosity about three times fainter than the results presented here. The equivalent star formation rate at redshift 5.7 is just  $0.79 f_{Ly\alpha}^{-1} M_\odot \text{ yr}^{-1}$ .

The biggest shortcoming of MNS is the time required to confirm candidates. Most of the emission-lines discovered with both MNS and NB imaging come from foreground galaxies. Narrowband imaging surveys parse the LAE candidate list using broadband colors and line equivalent width prior to spectroscopic confirmation. Broadband surveys of the requisite area, however, do not go deep enough to identify the continuum counterparts of many emission-line galaxies discovered with MNS. Broadband depth will be less of a problem for differential imaging, another special technique under development for LAE surveys, because the field of view is contiguous and therefore of smaller extent for a given survey area. A good example is the 6'8 by 6'8 field of DAZzLE (Dark Ages redshift Ly $\alpha$  Explorer, Horton et al. 2004) which subtends an area similar to that of our Venetian blinds mask and will be used to search for LAEs at  $z \sim 8 - 10$ .

Possible solutions for rapid identification of LAEs from MNS data include resolved line profiles and equivalent widths. Recognizing the red skew of high-redshift Ly $\alpha$  emission lines requires fairly high spectral resolution. The DEEP2 redshift survey provides a good example. Spectra were mostly taken with a 1200 line  $\text{mm}^{-1}$  grating. The observations targetted  $z \sim 1$  galaxies with multislit masks, but the “sky” regions of the slitlets subtend an area similar to our pilot survey. Sawicki et al. (2008) demonstrate that LAEs can be culled from the serendipitous detections of emission-line galaxies in the “sky” slits based on the shape of the line profile *and* the absence of additional emission lines. This second criterion is eliminated for MNS, and measurements of line asymmetry may become ambiguous at low signal-to-noise ratio. Deeper broadband imaging in even a single band longward of the emission line appears to be the fastest way to parse the emission-line candidates, as emission equivalent widths will normally be very high for Ly $\alpha$  due to the combination of the  $(1+z)$  boost and the potentially young, metal-poor stellar population.

### 5.1.2. Tunable Filters

Imaging observations with tunable filters can provide the same sensitivity and survey volume as MNS. The sky noise is comparable when the filter is cut down to the spectral resolution element of the MNS survey. The survey volumes will also be identical. While MNS slices the field spatially, it observes the entire redshift depth of the atmospheric window at once. Tunable filters image the whole field at once – one redshift slice at a time. The spatial and spectral slices are the same fraction of the volume for observations with the same camera and spectral resolution. The advantage of imaging is exact positional information for the emission-line sources. The position – wavelength degeneracy inherent to MNS will present ambiguities when sources need to be identified in deep continuum images.

We have taken data in the COSMOS field with the recently commissioned Maryland-Magellan Tunable Filter (MMTF) on IMACS. The highest resolution in the 8200Å is about 12Å, similar to our IMACS-MNS survey. We found a slightly higher throughput with the grism than the etalon, all other optical elements are the same. At redshift 5.7 both search techniques are viable for future searches, with the MMTF offering better positional information and MNS offering factor of 1.5-2.0 better line sensitivity. Further to the red, the OH-free windows are narrower; and tunable filters offer a substantial advantage over MNS. Although the MMTF is not sensitive beyond the 9000 – 9250Å atmospheric window, other Fabry Perot spectrographs will be. The Flamingos-2 Tandem TF (F2T2) is an infrared-optimized scanning TF, which will be mounted inside the Flamingos-2 imaging spectrograph of Gemini south. The spectral resolution of  $\Delta V \sim 375 \text{ km s}^{-1}$  will deliver broader lines than optimal but will likely offer an efficient ground-based survey strategy at  $z > 7$  in the near future.

### 5.2. Relation to Next-Generation Facilities

Spectroscopy with the next-generation of large ground-based telescopes will reach extraordinary sensitivity for

<sup>9</sup> The higher dispersion requires a larger separation between slits. The increase in depth is a single pointing is cancelled by the increase in the number of pointings required to map the full aperture of an imaging survey.

emission-lines in the airglow band gaps. The gain from diffraction-limited images will be as important as the increased aperture. Relative to our IMACS MNS survey (subscript ‘‘P’’ for pilot), MNS observations with a next-generation ground based telescope of aperture  $D$  could reach

$$F_{30m} = F_P / C_{Strehl} \sqrt{\frac{A_P}{A_{30m}} \frac{\theta_{30m}^2}{\theta_P^2}} \approx (D_P/30)^2 F_P, \quad (8)$$

where  $C_{Strehl}$  refers to the fraction of total light from an object in a circular aperture of diameter  $\theta$  and is related to the Strehl ratio.<sup>10</sup>

With adaptive optics and a 30 m aperture, line fluxes 21 times fainter than our IMACS observations become detectable. This sensitivity reaches SFRs of  $0.11 f_{Ly\alpha}^{-1} M_\odot \text{ yr}^{-1}$  at redshift 5.7 in 10 hours. Such a population may include the massive, young star clusters whose relics we see as the globular cluster population of the Milky Way today.

Next generation surveys may actually detect fainter line fluxes from higher redshift objects. First, the image quality delivered by adaptive optics will be better at longer wavelengths. Second, at high spectral resolution, the inter-hydroxyl-line background falls slowly with increasing wavelength between the 8200Å bandpass and 1.9  $\mu\text{m}$ .<sup>11</sup> Ground-based line searches should become extremely sensitive to emission lines from redshift 5.7 to 15. Longward of 2  $\mu\text{m}$ , thermal emission causes the background to rise and observations with JWST will have a strong advantage.

The ionized regions at redshift 7 to 10 will be mapped out by pointing these large telescopes at bright LAEs and finding fainter LAEs in the ionized bubbles. The Ly $\alpha$  line will only be transmitted through the IGM when the source is surrounded by an ionized bubble (Furlanetto & Oh 2005). An imaging tunable-filter, although not presently planned for first-light instrumentation on a 30m, could be the instrument of choice for such surveys. A more popular option for a facility instrument may be sets of deployable integral field units. A combined field-of-view exceeding 6''  $\times$  6'' could map the HII regions and provide spectral resolution or coverage for flagging interlopers.

The extreme sensitivities attainable at the diffraction limit will only be realized if some Ly $\alpha$  emission regions are small,  $\lesssim 50$  pc. Some theoretical models do predict small sizes (Le Delliou et al. 2006), but Ly $\alpha$  emission halos could also be quite extended. Empirical scaling relations for nearby HII regions,  $R_{HII} \propto \sigma^2$  (Terlevich & Melnick 1981), suggest we should expect narrow lines of width  $\lesssim 40 \text{ km s}^{-1}$  FWHM for small LAEs near the detection limit. The progenitors of the Milky Way’s globular cluster systems could plausibly be detected as young star clusters.

### 5.2.1. Ground-Based Emission-Line Sensitivity vs. JWST

Observations from the James Webb Space Telescope will not be hindered by telluric-OH emission, which is produced in a layer of atmosphere at roughly 87 km, or absorption by molecules in earth’s atmosphere, which precludes observations over about 20% of the 1-5  $\mu\text{m}$  region. The background from space is dominated by sunlight scattered off zodiacal dust and is strongly dependent on ecliptic latitude and longitude. Average values are about 10% as bright as the Maihara (1993) model for the interline background from the ground, although ‘‘deep fields’’ will presumably be carried out in regions of minimum zodi.

The JWST instruments FGS-TFI and NIRSpec provide the highest sensitivity to line emission. The planned configurations of these instruments do not minimize sky background. A single MEMS aperture on NIRSpec is much larger than a point source, and the spectral resolution of the Fabry Perot will not resolve line emission from galaxies. These designs reflect the dominance of detector noise over shot noise from the sky for many observations. Because JWST will be cooled to  $< 50$  K, emission-line observations with JWST will have their biggest advantage over ground-based line surveys at  $\lambda > 2 \mu\text{m}$ . The background (in frequency units) should reach a minimum between 3 and 4  $\mu\text{m}$  due to the slow decline of the zodiacal background with wavelength. In addition to extending studies of LAEs to redshift 30, the redder (and line-free) spectral coverage will be critical for studying hydrogen Balmer emission from objects toward the end of Reionization.

Emission-line observations at  $z < 15$  with JWST will not be restricted to OH-free bandpasses but are unlikely to be as sensitive as ground-based spectroscopy with a 30 m class telescope. Using the background-limited case for scaling, the limiting flux from space relative to a 30 m telescope is

$$F_{JWST} = F_{30m} C_{Strehl} \sqrt{\frac{\Sigma_{JW}}{\Sigma_{30}} \frac{A_{30}}{A_{JW}} \frac{\Delta\lambda_{JW}}{\Delta\lambda_{30}} \left(\frac{\theta_{JW}}{\theta_{30}}\right)^2}. \quad (9)$$

Assuming a relative sky brightness,  $\Sigma_{30}/\Sigma_{JW} \sim 10$ , ground-based spectroscopy could detect lines about a factor of five fainter than JWST if the diffraction limit of a 30 m telescope can be reached. The line sensitivity of these two telescopes is comparable at equivalent spectral resolution and image quality; the extra collecting area roughly canceling the brighter sky. Even in the JWST era, large ground-based telescopes may lead the search to map the progression of reionization with LAEs.

## 6. SUMMARY

This paper presents the first LAEs discovered with narrowband, multislit spectroscopy. The technique succeeds on the 6.5 m Baade telescope because of the large detector on IMACS and its wide field-of-view. Our configuration reduced the sky noise by a factor of 10 relative to imaging through the same narrowband filter and provided spatial multiplexing 100 times that of a single longslit observation. The faintest confirmed LAE in the pilot survey has an ob-

<sup>10</sup> The Strehl ratio refers specifically to the ratio of peak intensity from a point source to the maximum intensity in a diffraction limited image with the same total flux.

<sup>11</sup> The Gemini ITC background model suggest the between-the-lines background in units of  $\Sigma_\nu$  reaches a maximum in J band (around 1.25  $\mu\text{m}$ ) which is about three times the 8200Å background. Converting from frequency units to wavelength units cancels this out,  $\frac{\Sigma_\lambda(1.25)}{\Sigma_\lambda(0.82)} = 0.43 \frac{\Sigma_\nu(1.25)}{\Sigma_\nu(0.82)}$ .

served line flux of  $F_{Ly\alpha} = 1.4 \pm 0.2 \times 10^{-17}$  erg s $^{-1}$  cm $^{-2}$ , which is near the estimated 90% completeness limit.

The three redshift 5.7 LAEs have luminosities  $L_{Ly\alpha} \geq 5 \times 10^{42}$  erg s $^{-1}$ , which correspond to star formation rates greater than 5-7  $M_{\odot}$  yr $^{-1}$  (for Salpeter IMF from 0.1 to 100  $M_{\odot}$  and solar metallicity). The fraction of intrinsic Ly $\alpha$  emission absorbed by the galactic ISM likely varies with age and wind strength, while intervening IGM will absorb the Ly $\alpha$  photons emitted blueward of the line center, contributing to the red skew of the line profile. The true star formation rates could easily be closer to 10-30  $M_{\odot}$  yr $^{-1}$ . Winds with speeds of a few hundred km s $^{-1}$  are common among local galaxies with star formation rates comparable to these LAEs and are consistent with the red wing of Ly $\alpha$  line profile. The rest-frame ultraviolet continuum of these LAEs is fainter than the sensitivity limits of current wide-angle surveys. Future broadband measurements will constrain the age, mass, and dust content of these galaxies. Their relation to the i-dropout population is likely complex, although our best estimate of the cumulative Ly $\alpha$  luminosity distribution is consistent with being drawn from the i-dropout population around redshift 6.

Results from the IMACS MNS survey tightly constrain the product of the luminosity function parameters  $L_{*,Ly\alpha}$  and  $\phi_{*,Ly\alpha}$ . Nearly all candidates were followed up with both low- and high- resolution spectroscopy. The LAE population detected to date is unlikely to supply enough Lyman continuum photons to maintain the ionization of the IGM at redshift 5.7. For this detected population of LAEs to ionize the IGM, both a low value of the break luminosity ( and therefore a high normalization) and a combination of clumping, attenuation, and escape factors yielding  $\zeta \approx 0.1$ , where  $\zeta \equiv C_6(1 - 0.1f_{LyC,0.1})f_{Ly\alpha,0.5}f_{LyC,0.1}^{-1}$ , would have to be realized. Determining whether galaxies ionize the IGM will clearly require deeper surveys that pin down the luminosity function parameters.

Deeper emission-line surveys in the OH-free bandpass at 8200Å are possible with either MNS or the MMTF at Magellan. The former approach offers maximum depth while

the tunable filter offers more accurate source positions. Both methods probe the same volume per pointing, which is much larger than the volume strongly lensed by a cluster. These techniques can be used on Magellan to reach lines 2-4 times fainter than the results presented here. Such depth over a large volume should remove ambiguity about the value of  $L_{*,Ly\alpha}$ , particularly if complemented by shallower surveys with the volume to count LAEs brighter than  $\log L_{Ly\alpha}(\text{erg s}^{-1}) = 43$ .

Emission-line sensitivities will likely need to be improved further to find both the sources responsible for reionization and those that prevent the IGM from recombining at  $z \sim 6$ . Finding these sources is a key science goal of the JWST mission. The next generation of ground-based telescopes with primary mirrors  $\sim 30$  m in diameter (and adaptive optics) will offer even higher sensitivity to line emission shortward of  $2\mu\text{m}$ , extending LAE searches to redshift 15 and detecting other lines like HeII 1640 at lower redshift. Our experiences with MNS indicate that isolated lines, lines with very large observed equivalent widths, and lines with red-skewed, asymmetric profiles are not exclusively Ly $\alpha$ . Culling or exploiting the large number of foreground emission-line galaxies from samples will have to be a key part of any experimental design. While identification of the Lyman break is one robust method, it obviates one perk of line searches, which is discovering objects below the detection limit of continuum surveys.

We thank Peter Capak for discussions of the COSMOS observations, Bahram Mobasher for his photometric-redshift catalog, Hsiao-Wen Chen for computing limiting sensitivities of the LCIRS images, and Richard Ellis, Rychard Bouwens, and an anonymous referee for helpful comments on the manuscript. C.L.M. is grateful for the lively environment of the Kavli Institute for Theoretical Physics, where the manuscript was completed. This work was supported in part by the David and Lucile Packard Foundation, the Alfred P. Sloan Foundation, and the National Science Foundation under Grant No. PHY05-51164.

*Facilities:* Magellan, Keck

## REFERENCES

- Ahn, S., Lee, H., Lee, H. M. 2003, MNRAS, 340, 863  
 Ajiki, M. et al. 2003, AJ, 126, 2091  
 Ajiki, M. et al. 2004, PASP, 56, 597  
 Ajiki, M. et al. 2006, ApJ, 638, 596  
 Becker, G. et al. 2006, ApJ, 640, 69  
 Becker, G., Rauch, M., & Sargent, W. L. W. et al. 2007, ApJ, 662, 72  
 Becker, R. H. et al. 2001, AJ, 122, 285  
 Beckwith, S. et al. 2006, AJ, 132, 1729  
 Benson, A. J. et al. 2002, MNRAS, 333, 177  
 Bertin & Arnouts 1996, A&AS, 117, 393  
 Bland-Hawthorn, J. & Englund, M. 2004, Optics Express, 12, 24, 5902  
 Bouwens, R. J. et al. 2007, astro-ph/0707.2080  
 Bouwens, R. J. et al. 2006, 653, 53  
 Brocklehurst, M. 1971, MNRAS, 153, 471  
 Chen, H.-W. et al. 2002, ApJ, 570, 54  
 Chen, H.-W., Prochaska, J. X. & Gnedin, N. Y. 2007, ApJ, 667, 125  
 Crampton, D. & Lilly, S. 1999, ASP Conf. Series, 191, p. 229  
 Cuby, J. G. et al. 2003, A&A, 405, L19  
 Dawson, S. et al. 2002, 570, 92  
 Dawson, S. 2004, ApJ, 617, 707  
 Dawson, S. et al. 2007, ApJ, 671, 1227  
 Le Delliou, M. et al. 2006, MNRAS, 365, 712  
 Dijkstra, M., Haiman, Z., & Spaans, M. 2006, ApJ, 649, 37  
 Djorgovski, S. G. et al. 2001, ApJ, 560, 5  
 Dow-Hygelund, C. C. et al. 2007, ApJ, 660, 47  
 Dressler, A. et al. 2006, SPIE, 6269, 13  
 Ellis, R. et al. 2001, ApJ, 560, L119  
 Fan, X. et al. 2002, AJ, 123, 1247  
 Fan, X., Carilli, C. L., & Keating, B. 2006, ARA&A, 44, 415  
 Felten, J. E. 1976, ApJ, 207, 700  
 Fernandez-Soto, A., Lanzetta, K. M., and Chen, H.-W. 2003, MNRAS, 342, 1215  
 Fujita, A. et al. 2003, ApJ, 599, 50  
 Furlanetto, S. & Oh, P. 2005, MNRAS, 363, 1031  
 Gehrels, N. 1986, ApJ303, 336  
 Giallongo, E. et al. 2002, ApJ, 568, L9  
 Glazebrook, K. & Economou, R. 1997, The Perl Journal, 5, 5  
 Gnedin, N. 2007, arXiv:0709.3308  
 Gronwall, C. et al. 2007, ApJ, 667, 79  
 Hansen, M. & Oh, P. 2006, MNRAS, 367, 979  
 Hauser, M. et al. 1998, ApJ, 508, 25  
 Horton, A. et al. 2004, SPIE, 5492, 1022  
 Hu, E. et al. 2002, ApJ, 568, L75  
 Hu, E. et al. 2004, AJ, 127, 563  
 Hurwitz, M. et al. 1997, ApJ, 481, 31  
 Inoue, A. K. et al. 2005, A&A, 435, 471  
 Iwata, I. et al. 2007, MNRAS, 376, 1557  
 Iye, M. 2006, Nature, 443, 186  
 Kashikawa, N. et al. 2006, ApJ, 648, 7  
 Kelsall, T. et al. 1998, ApJ, 508, 44

- Kennicutt, R. C. 1998, *ARA&A*, 36, 189  
Kodaira, K. et al. 2003, *PASJ*, 55, 17  
Madau, P. 1995, *ApJ*, 441, 18  
Madau, P. et al. 1999, *ApJ*, 514, 648  
Maihara, T. et 1993, *PASP*, 105, 940  
Malhotra, S. & Rhoads, J. E. 2002, *ApJ*, 565, 71  
Malhotra, S. & Rhoads, J. E. 2004, *ApJ*, 617, L5  
Martin & Sawicki 2004, *ApJ*, 603, 414  
Marzke, R. O. et al. 1999, in *ASP Conf. Ser.* 191, *Photometric Redshifts and the Detection of High Redshift Galaxies*, ed. R. Weymann, L. Storrie-Lombardi, M. Sawicki, & R. Brunner (San Francisco: ASP), 148  
Mobasher, B. et al. 2007, *ApJ*, also *astro-ph/0612344*  
Murayama, T. et al. 2007, *ApJS*, 172, 523  
Oke, J. B., et al. 1995, *PASP*, 107, 375  
Ouchi, M. et al. 2003, *ApJ*, 582, 60  
Ouchi, M. et al. 2007, *arXiv0707.3161*  
Page, L. et al. 2006, *ApJS*, 170, 335  
Pirzkal, N. et al. 2007, *ApJ*, 667, 49  
Rhoads, J. E. et al. 2004, *ApJ*, 611, 59  
Rhoads, J. E. & Malhotra, S. 2001, *ApJ*, 563, 5  
Ryan-Weber, E., Pettini, M., & Madau, P. 2006, *MNRAS*, 371, L78  
Santos, M. R. et al. 2004, *ApJ*, 606, 683  
Sawicki, M. et al. 2007, submitted to *ApJ*  
Schaerer, D. 2007, *arXiv:0706.0139*  
Scoville, N. et al. 2007, *ApJS*, 172, 38  
Shapley, A. E. et al. 2003, *ApJ*, 588, 65  
Shapley, A. E. et al. 2006, *ApJ*, 651, 888  
Shimasaku, K. et al. 2006, *PASJ*, 58, 313  
Simcoe, R. 2006, *ApJ*, 653, 977  
Songaila, A. 2004, *AJ*, 127, 2598  
Spergel, D. N. 2007, *ApJS*, 170, 377  
Stanway, E. R. et al. 2007, *MNRAS*, 376, 727  
Stark, D. P. et al. 2007a, *ApJ*, 659, 84  
Stark, D. P. et al. 2007b, *ApJ*, 663, 10  
Stark, D. P., Loeb, A., & Ellis, R. S. 2007, *ApJ*, 668, 627  
Steidel, C., Pettini, M., and Adelberger, K. L. 2001, *ApJ*, 546, 665  
Stern, D. et al. 2005, *ApJ*, 619, 12  
Tapken, C. et al. 2007, *A&A*, 467, 63  
Taniguchi, Y. et al. 2005, *PASJ*, 57, 165  
Taniguchi, Y. et al. 2007, *ApJS*, 172, 9  
Tran et al. 2004, *ApJ*, 612, 89  
Trenti, M. & Stiavelli, M. 2007, *arXiv0712.0398*  
Verhamme, A., Schaerer, D., et al. Maselli, A. 2006, *A&A*, 460, 397  
Westra, E. 2006, *A&A*, 455, 61  
Westra, E. 2005, *A&A*, 430, L21  
Xu, C. 2007, *AJ*, 134, 169

TABLE 1  
MAGELLAN MULTISLIT, NARROWBAND EMISSION-LINE SURVEY

Date	Mask	RA (J2000)	DEC (J2000)	Slit PA ( $^{\circ}$ )	Exposure (hr)	Clouds/ Image Quality
2004 April	COSMOS-0	10:00:42.9	+02:11:00	90	6.33	Clear; 0.8-2.5''
2004 April	15H Field-0	15:23:35.48	-00:08:00.00	135	10.8	Clear; 0.8-2.5''
2005 March	COSMOS-0.5	10:00:42.9	+02:11:00	90	10.0	Clear; 0.6-0.8''
2005 May	15H Field-0.5	15:23:35.48	-00:08:00.00	135	6.75	Thin Clouds; 0.6-0.8''

TABLE 2  
CANDIDATE YIELD AND SPECTROSCOPIC CLASSIFICATION

(1) Survey	(2) Confirmed LAEs	(3) Confirmed Single Line	(4) Foreground Objects	(5) No Follow Up	(6) Not Recovered
10H 2004 - Line Only	1	7	20	3	5
10H 2005 - Line Only	0	2	27	1	3
15H 2004 - Line Only	1	6	25	6	4
15H 2005 - Line Only	1	1	19	1	3
10H 2004 - Line + Cont.	0	0	18	16	1
10H 2005 - Line + Cont.	0	0	20	12	4
15H 2004 - Line + Cont.	0	0	21	11	8
15H 2005 - Line + Cont.	0	0	19	0	1

Note. — Cols – (1) Survey name and description of the continuum flux in the NB8190 band. (2) Number of confirmed LAEs. (3) Number of LAE candidates confirmed to be single-line sources. (4) Number of lines in 8190 band identified as foreground objects. (5) Number of emission-line objects not followed up. (6) The Number of emission-line objects not redetected. Note that exposure times of follow vary.

TABLE 3  
LAE CANDIDATES

(1) Name	(2) RA (J2000.0)	(3) DEC (J2000.0)	(4) F(Lya) ( $\text{erg s}^{-1} \text{cm}^{-2}$ )	(5) $W_o$ ( $\text{\AA}$ )	(6) $\lambda_o$ ( $\text{\AA}$ )
MSDM80+3	10:00:30.479	02:17:14.80	$14 \pm 2 \times 10^{-18}$	> 244	8141
MSDM64-5	10:01:12.769	02:13:14.80	$63 \pm 8 \times 10^{-18}$	> 1082	8141
MSDM13-3	10:00:54.458	02:00:30.67	$14 \pm 2 \times 10^{-18}$	> 240	8169
MSDM50-7	10:01:23.675	02:09:45.15	$16 \pm 4 \times 10^{-18}$	> 281	8122
MSDM52+8	09:59:53.266	02:10:15.11	$25 \times 10^{-18}$	421	8179
MSDM30.5-8	10:01:29.407	02:04:53.60	$26 \pm 8 \times 10^{-18}$	> 447	8173
MSDM17.5+8	10:00:08.176	02:01:38.46	$43 \pm 9 \times 10^{-18}$	> 739	8129
MSDM17-1	10:00:45.109	02:01:30.41	$32 \pm 2 \times 10^{-18}$	> 555	8162
MSDM29.5+5	15:22:57.880	-00:07:36.34	$18 \pm 2 \times 10^{-18}$	...	8148
MSDM71-5	15:24:08.929	-00:10:43.06	$22 \pm 6 \times 10^{-18}$	> 61	8130
MSDM89-2	15:24:03.935	-00:03:06.53	$14 \pm 5 \times 10^{-18}$	> 39	8200
MSDM57+4	15:23:19.653	-00:03:20.27	$21 \pm 6 \times 10^{-18}$	> 58	8178
MSDM36+5	15:23:03.246	-00:06:38.71	$17 \pm 8 \times 10^{-18}$	> 47	8135
MSDM54.5-1	15:23:37.234	-00:08:36.91	$11 \pm 6 \times 10^{-18}$	> 31	8222
MSDM55-3	15:23:48.230	-00:11:11.24	$4.9 \pm 5 \times 10^{-18}$	> 14	8170
MSDM94-4	15:24:15.670	-00:04:16.34	$9.5 \pm 7 \times 10^{-18}$	> 26	8144
MSDM70+1	15:23:44.420	-00:04:56.60	$9.4 \pm 5 \times 10^{-18}$	> 26	8227

NOTES - In addition to confirmed LAEs MSDM80+3, MSDM29.5+5, and MSDM71-5, we list candidates presenting a single line in our low resolution follow-up spectra. (col 1) - Object Name. Format is MSDM[Slit Number].[Field Identifier][ $\pm$ Slit Segment]. (col 2, 3) - Coordinates. See § 2.1 for full description of uncertainties. (col 4) - Line flux measured in search image. (col 5) - Measured emission equivalent width in the observed frame. An upper limit on the continuum flux density of  $5.8 \times 10^{-20}$  and  $3.6 \times 10^{-19} \text{ erg s}^{-1} \text{ cm}^{-2} \text{ \AA}^{-1}$  is assumed for the 10H Subaru  $z'$  imaging and the 15H LCIRS  $z'$  imaging, respectively. An entry of nodata indicates that this imaging does not cover the position of the object. (col 6) - Wavelength measured in follow-up spectrum. The uncertainty is dominated by the placement of the object in the  $1''.5$  slit. One half the slit width corresponds to a wavelength uncertainty of about  $7''.5$ .

TABLE 4  
CUMULATIVE LUMINOSITY DISTRIBUTION OF LAES

F	L	V	$\phi(> L)$ 95%CL	$\phi(> L)$ 84.1% CL
( $\text{erg s}^{-1} \text{cm}^{-2}$ )	( $\text{erg s}^{-1}$ )	( $h_{70}^{-3} \text{Mpc}^{-3}$ )	( $h_{70}^3 \text{Mpc}^{-3}$ )	( $h_{70}^3 \text{Mpc}^{-3}$ )
$2.2 \times 10^{-17}$	$7.8 \times 10^{42}$	$4.429 \times 10^4$	$2.26^{+8.5}_{-2.1} \times 10^{-5}$	$2.26^{+5.2}_{-1.9} \times 10^{-5}$
$1.8 \times 10^{-17}$	$6.4 \times 10^{42}$	$3.904 \times 10^4$	$4.79^{+13}_{-3.2} \times 10^{-5}$	$4.79^{+7.9}_{-2.8} \times 10^{-5}$
$1.4 \times 10^{-17}$	$5.0 \times 10^{42}$	$2.402 \times 10^4$	$8.95^{+20}_{-5.1} \times 10^{-5}$	$8.95^{+12}_{-4.4} \times 10^{-5}$

Notes: Col(1) – Estimated line flux of LAE. Col(2) – Estimated Ly $\alpha$  luminosity. Col(3) Survey volume within which the object could have been detected. Col(4,5) Cumulative number density of LAEs computed from  $\phi(L \geq L_i) = \sum_j n_j = \sum_j (1/V_{m,j})$ , where the sum is over all galaxies  $j$  with  $L_j \geq L_i$ . We divide the Poisson error on 1 object by the volume  $V_j$  to get the error on each  $n_j = 1/V_j$  term. Following Gehrels (1986), the 84.1% (95%) confidence range for 1 detection is 0.173 to 3.300 (0.0513 to 4.744) objects, respectively. And the total error is  $\delta\phi = \delta(N = 1)[\sum_j (1/V_{m,j})^2]^{0.5}$ , where  $\delta(N = 1)$  takes the values +3.744 and -0.9487 objects (in column 4) and +2.300 and -0.827 objects (in column 5).

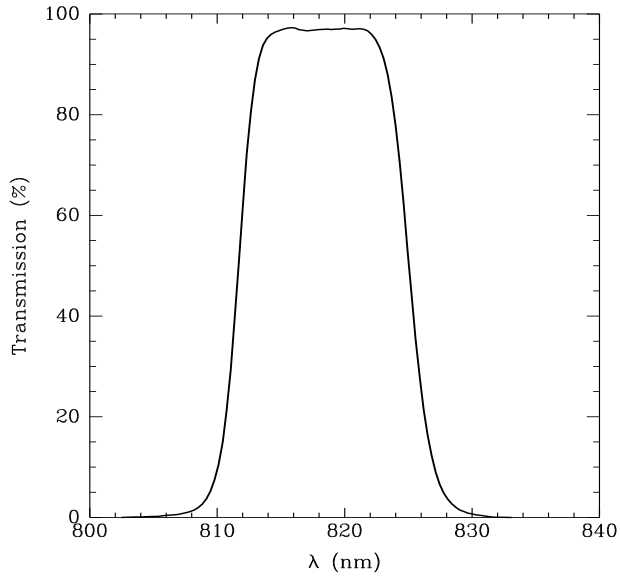


FIG. 1.— Transmission of the NB8190 filter.

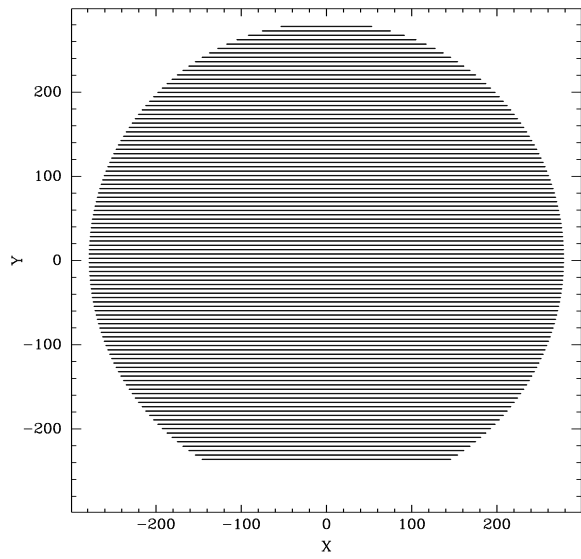


FIG. 2.— IMACS slit mask used for the spectroscopic survey. Coordinates denote positions in the focal plane. The  $1''.5$  wide slits subtend a geometric area of  $55.3 \square'$  per pointing within the  $27''.50$  diameter field of the camera.

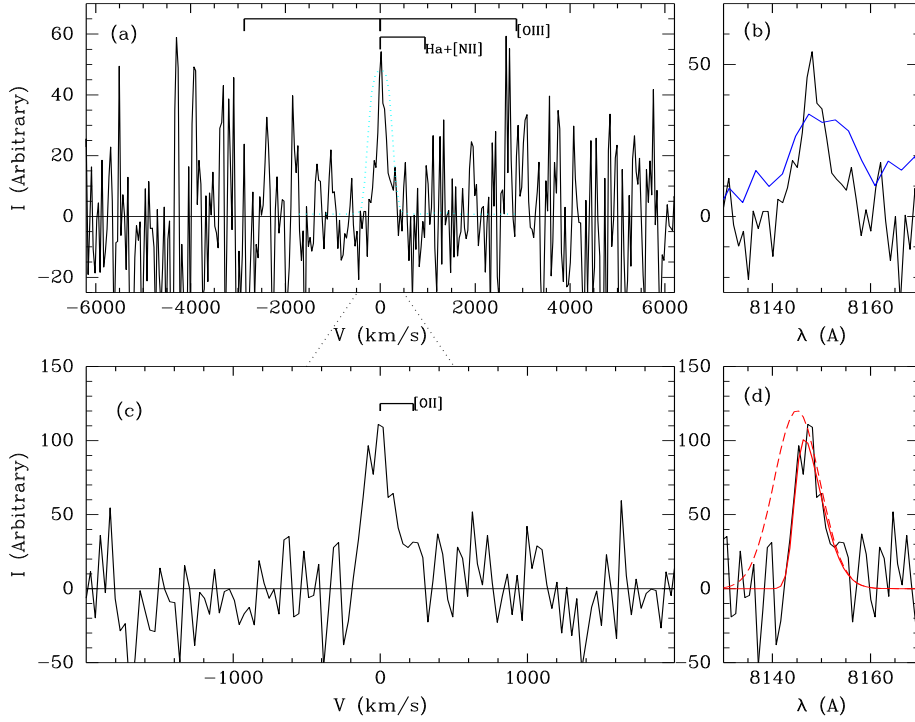


FIG. 3.— LAE MSDM29.5+5. The zeropoint of the velocity scale is arbitrary, defined with zero at maximum intensity for convenience. Ticks mark the separations of lines that commonly appear in our spectra of foreground interlopers. (a): IMACS 200-1 f/2 spectrum taken in 2005 June. The line is narrow compared to the profile of a sky line, shown by the light-blue, dotted line. (b): Spectrum from (a) on a wavelength scale. Also shown is an IMACS 150-1 f/2 spectrum taken in 2006 June (thick, blue line). (c): Higher resolution, Keck/LRIS spectrum. The line is asymmetric and skewed to the red. (d): Keck/LRIS spectrum and fit. The model is a Gaussian ( $400 \text{ km s}^{-1}$  FWHM) with flux blueward of the peak set to zero and then convolved with another Gaussian representing instrumental broadening ( $110 \text{ km s}^{-1}$ ).

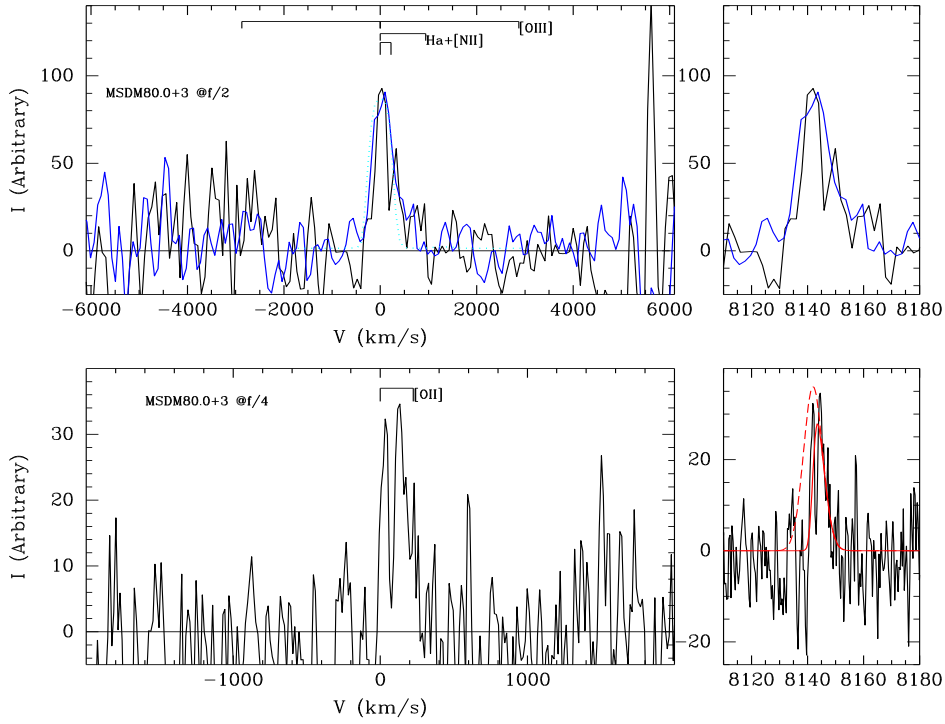


FIG. 4.— LAE MSDM80+3. Velocity scale, tic marks, and arc line as in Figure 3. *a, b*: IMACS  $f/2$  spectra from 2005 May (thin, white line) and 2007 February (thick, blue line). *c*: IMACS  $f/4$  spectrum. *d*: IMACS  $f/4$  spectrum and fit. The model is a Gaussian ( $330 \text{ km s}^{-1}$  FWHM) with flux blueward of the peak set to zero and a  $150 \text{ km s}^{-1}$  wide Gaussian  $330 \text{ km s}^{-1}$  redward of the first. These components were convolved with another Gaussian representing instrumental broadening ( $150 \text{ km s}^{-1}$ ).

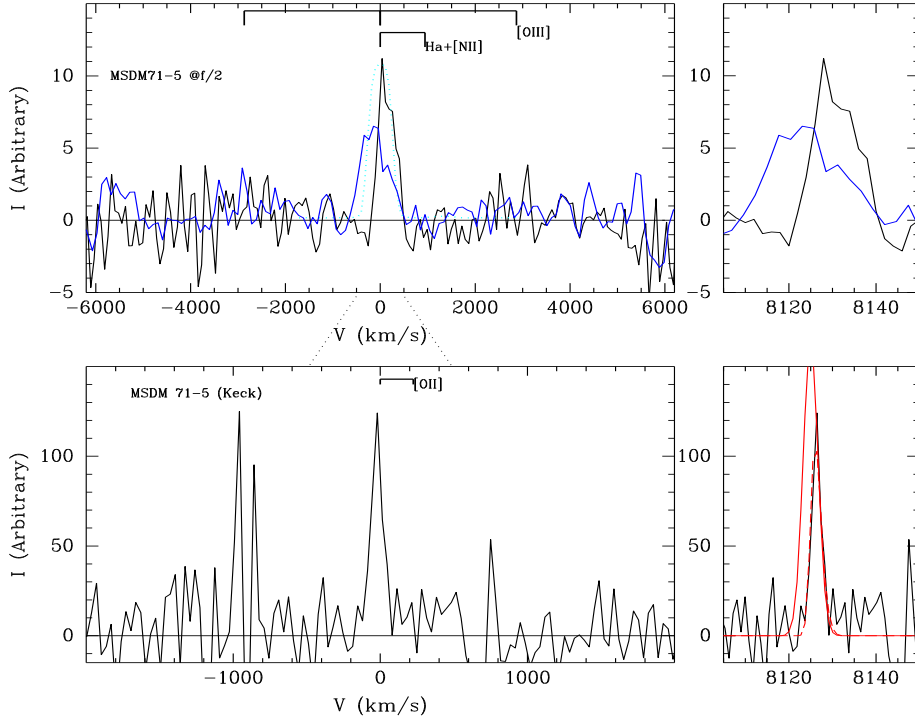


FIG. 5.— LAE MSDM71-5. Velocity scale, tic marks, and arc line as in Figure 3. *Top*: IMACS f/2 spectra with the 200-l grism in 2004 July (thin, white line) and the 150-l grism in 2006 June (thick, blue line). *Bottom*: IMACS f/4 spectrum. The model is a Gaussian ( $150 \text{ km s}^{-1}$  FWHM) with flux blueward of the peak set to zero and then smoothed by an instrumental response of width  $75 \text{ km s}^{-1}$ .

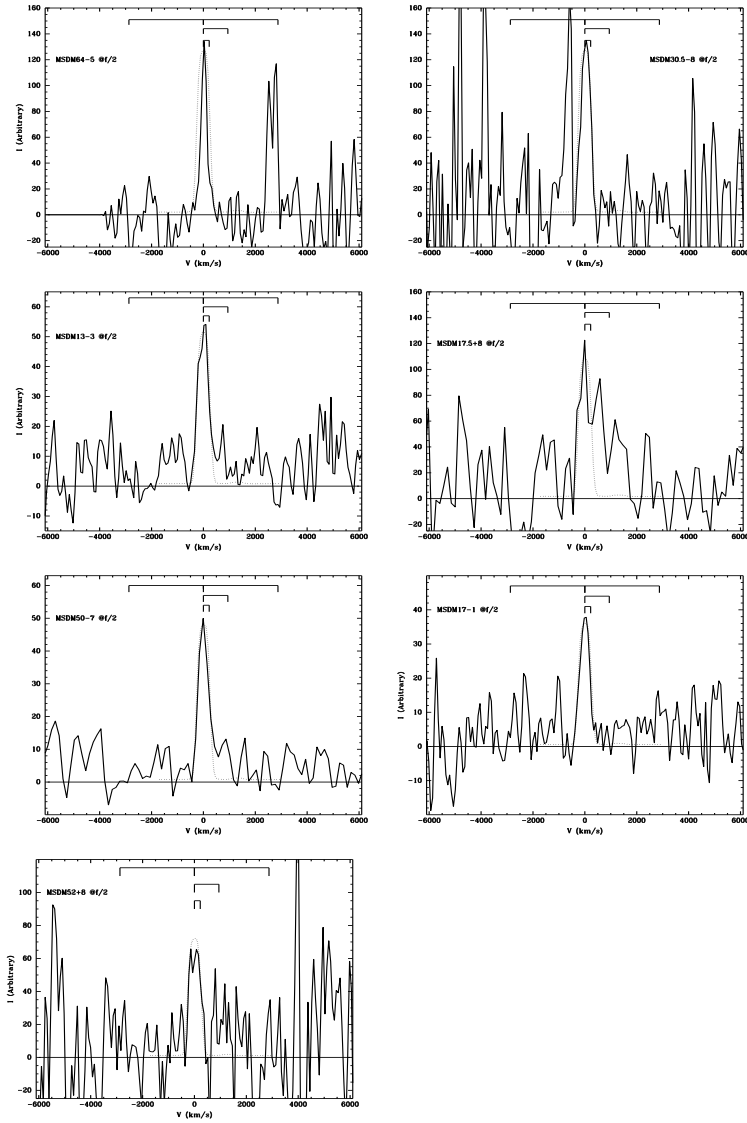


FIG. 6.— Low-resolution ( $f/2$ ) spectra of 10H Field LAE candidates. The objects shown have a single line in the observed-frame 5000-9000Å bandpass. This inset shows no lines are seen at the spacing (tic marks) of the foreground contaminants  $[\text{OIII}]5007,4959$  or  $\text{H}\alpha + [\text{NII}]6584$ . Comparison to the profile (dotted line) of a source that fills the slit shows the lines are unresolved, and higher resolution spectroscopy is required to show line asymmetry and/or identify the  $[\text{OII}] 3726,29$  doublet (small tics).

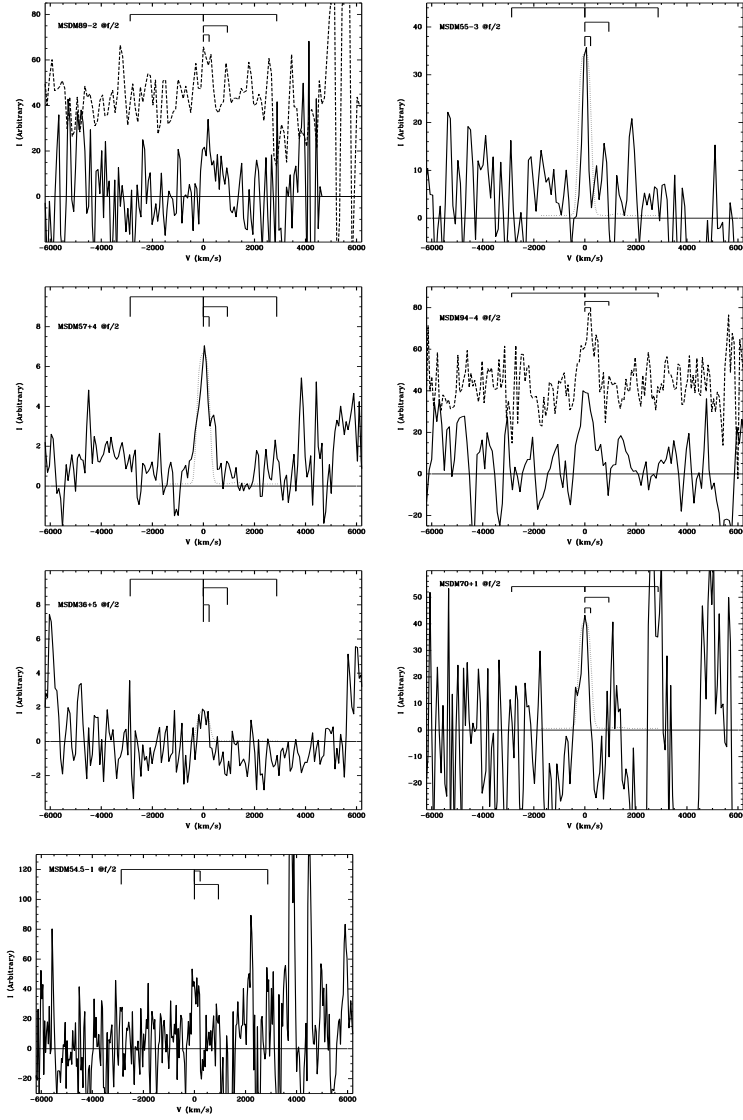


FIG. 7.— Low-resolution IMACS spectra of 15H Field LAE candidates. The objects shown have a single line in the observed-frame 5000-9000Å bandpass. This inset shows no lines are seen at the spacing (tic marks) of the foreground contaminants [OIII]5007,4959 or  $H\alpha + [NII]6584$ . Comparison to the profile (dotted line) of a source that fills the slit shows the lines are unresolved, and higher resolution spectroscopy is required to show line asymmetry and/or identify the [OII] 3726,29 doublet (small tics).

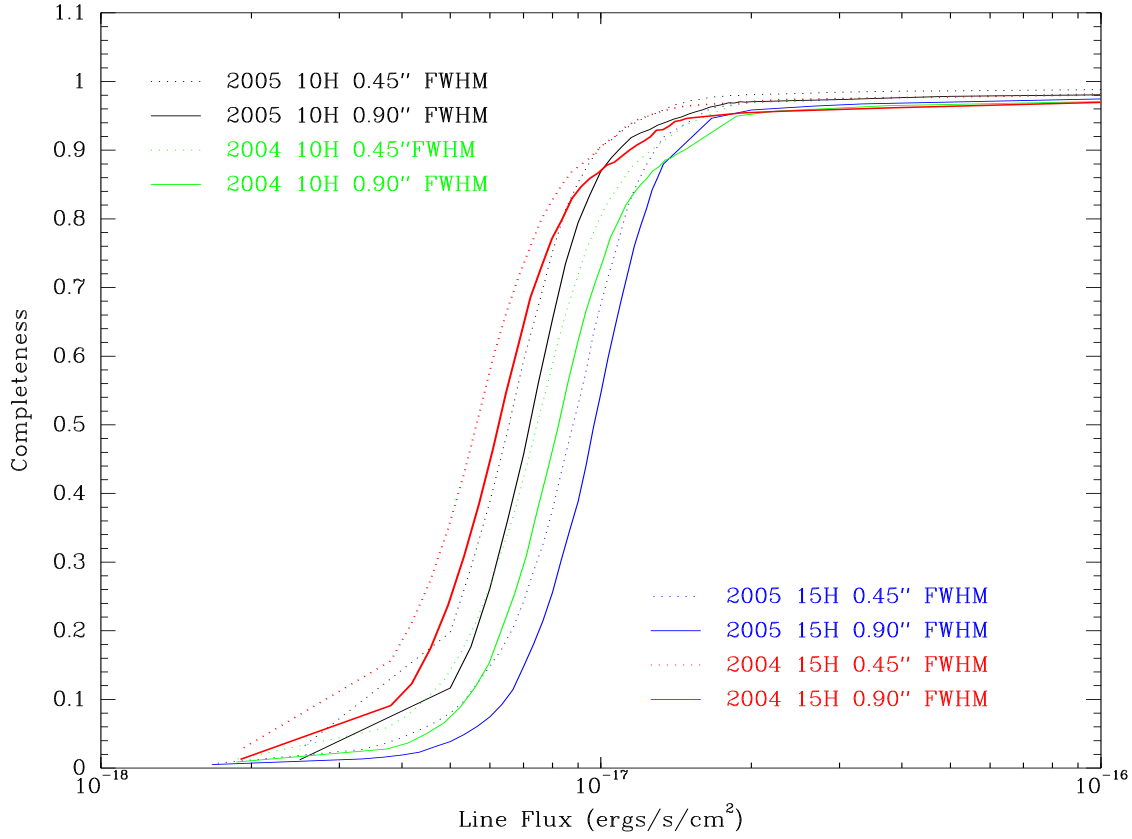


FIG. 8.— Completeness of emission-line surveys for two limiting source sizes. For the 2005 search in the 10H Field, the line flux corresponding to 50% completeness is  $6.6 - 7.2 \times 10^{-18} \text{ erg s}^{-1} \text{ cm}^{-2}$  for sources between  $0''.45$  and  $0''.90$  FWHM.

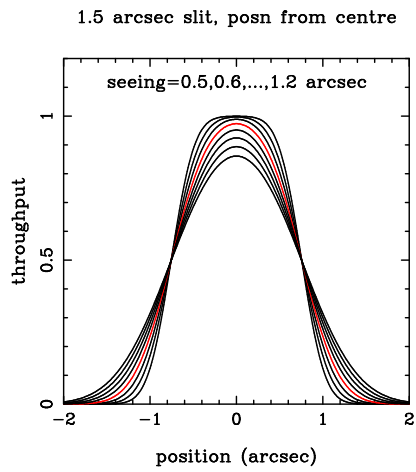


FIG. 9.— Attenuation of flux vs. offset from center of  $1''.5$  wide slit. Slit losses are shown for seeing-convolved sources with Gaussian surface brightness profiles of FWHM 0.5 to  $1''.2$  in steps from  $0''.1$ . The red curve represents the worst effective image quality in our survey.

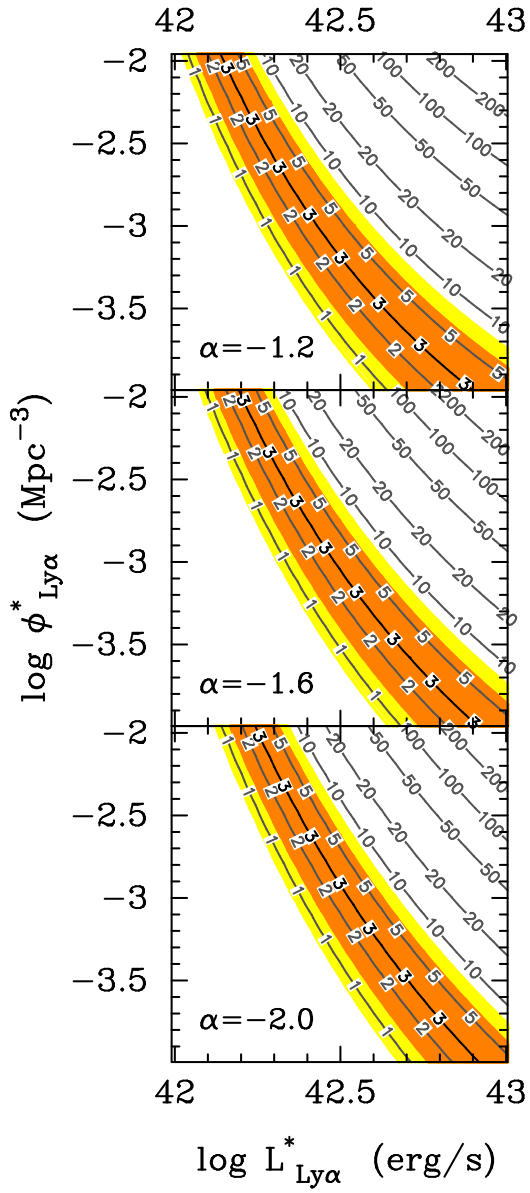


FIG. 10.— Mean number of LAEs detected in our experiment for different values of the intrinsic luminosity function parameters. From top to bottom, the panels show faint-end slope  $\alpha = -1.2, -1.6,$  and  $-2.0$ . The y-axis is the normalization of the luminosity function,  $\phi^*$ , The x-axis is the characteristic luminosity  $L_*$ . The orange and yellow shading marks the 84.1% and 95% confidence regions for detecting 3 LAEs.

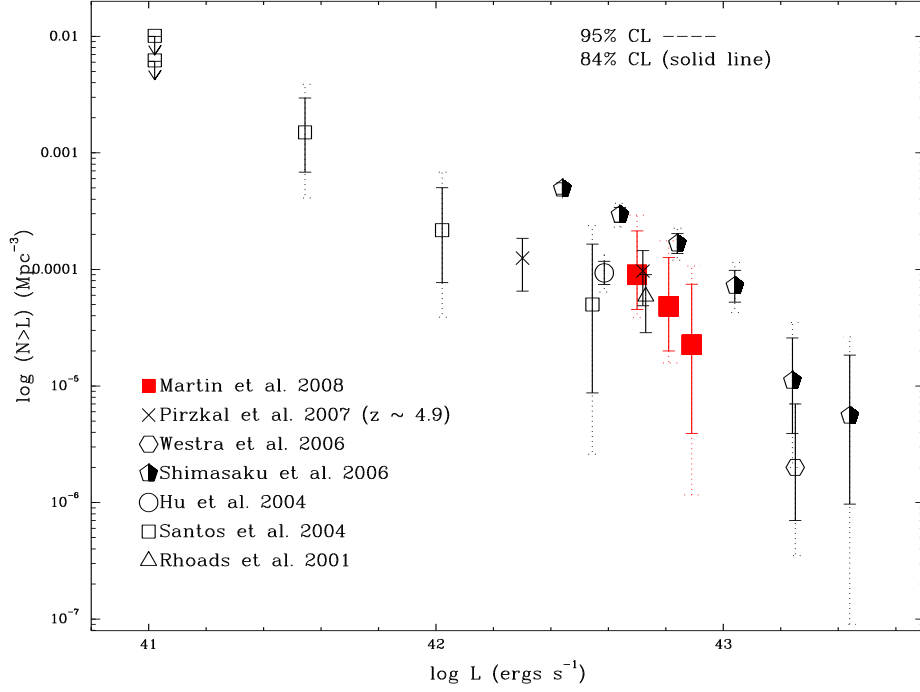


FIG. 11.— Cumulative number density of LAEs. Our best estimate is shown by the solid squares; the errorbars are discussed in the caption to Table 4. We compare number densities from the following narrowband imaging surveys: LALA 2001 (triangle), Hu et al. 2004 (circle), Westra et al. 2006 (hexagon), and Shimasaku et al. 2006 (pentagons). Spectroscopic results are shown from GRAPES (Pirzkal et al. 2007, crosse) and a program that positioned longslits along cluster caustics (Santos et al. 2004, open squares).

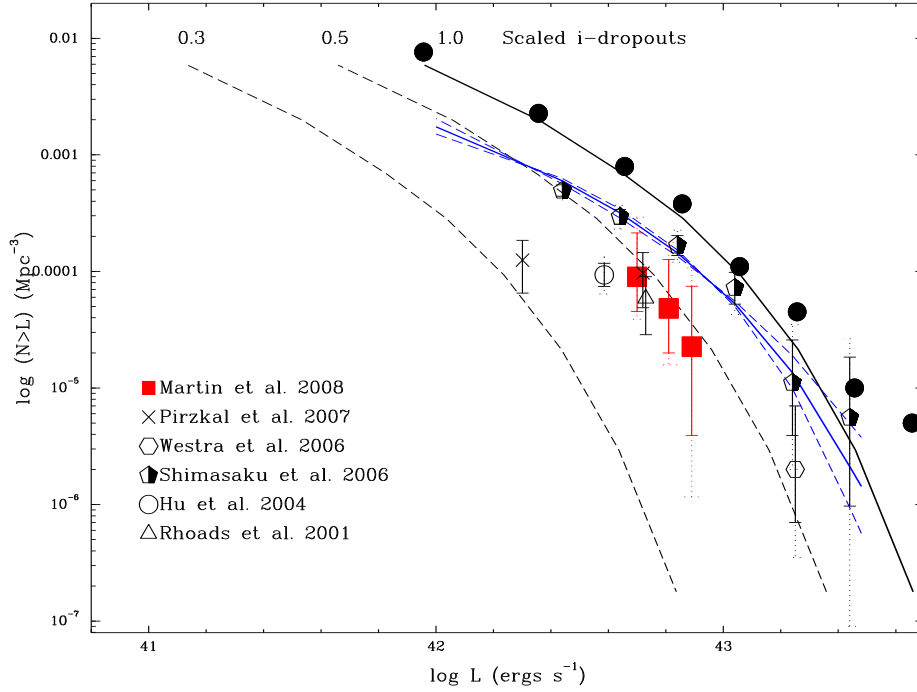


FIG. 12.— Comparison of cumulative number density of  $z = 5.7$  LAEs and i-dropouts. Blue curves show the fitted luminosity distribution of LAEs from Shimasaku et al. (2006) with faint-end slope  $\alpha = -2.0, -1.5$  (solid), and  $-1.0$ . Black curves show the adopted fit to the distribution of i-dropouts from Bouwens et al. (2007); for purposes of illustration, we adopt constant  $\text{Ly}\alpha$  escape fractions of  $f_{\text{Ly}\alpha} = 1.0, 0.5$ , and  $0.3$ . The dashed, black curve illustrates the magnitude of some systematic uncertainties in the luminosity distribution fit; and solid circles show the i-dropout counts, converted to  $\text{Ly}\alpha$  luminosity using  $f_{\text{Ly}\alpha} = 1.0$ .

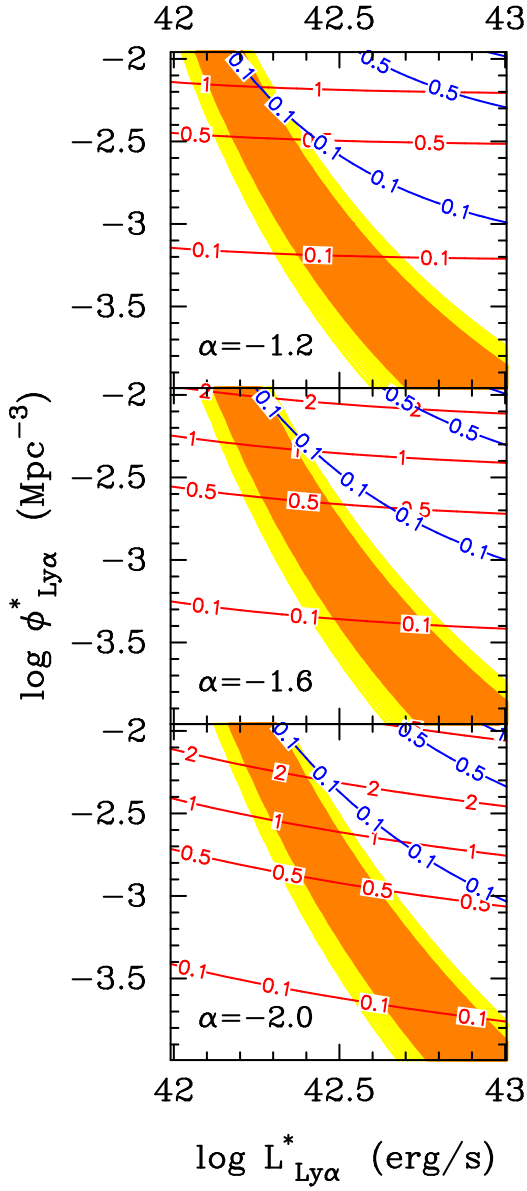


FIG. 13.— Total Ly $\alpha$  luminosity density for the 3 values of the faint-end slope. Two lower limits are illustrated: (1) our survey detection limit of  $\log L = 42.57 \text{ erg s}^{-1}$  (blue contours), and (2) an extrapolation to  $\log L = 41.00 \text{ erg s}^{-1}$  (red contours), which corresponds to dwarf galaxies with  $SFR = 0.095 f_{Ly\alpha}^{-1}$ . The critical number of sources required to keep the IGM ionized is marked in units of the parameters  $C_6(1 - 0.1 f_{LyC,0.1}) f_{Ly\alpha,0.5} / f_{LyC,0.1} = 1.0$ . With the lower limit in (1), it appears unlikely that enough galaxies have been discovered to keep the IGM ionized at  $z=5.7$ . It appears, however, from (2) that an extension of this population to lower luminosities, even with a shallow faint-end slope like  $\alpha = -1.2$ , could easily produce the missing ionizing photons.